Cell

mRNA 3′ UTRs chaperone intrinsically disordered regions to control protein activity

Graphical abstract

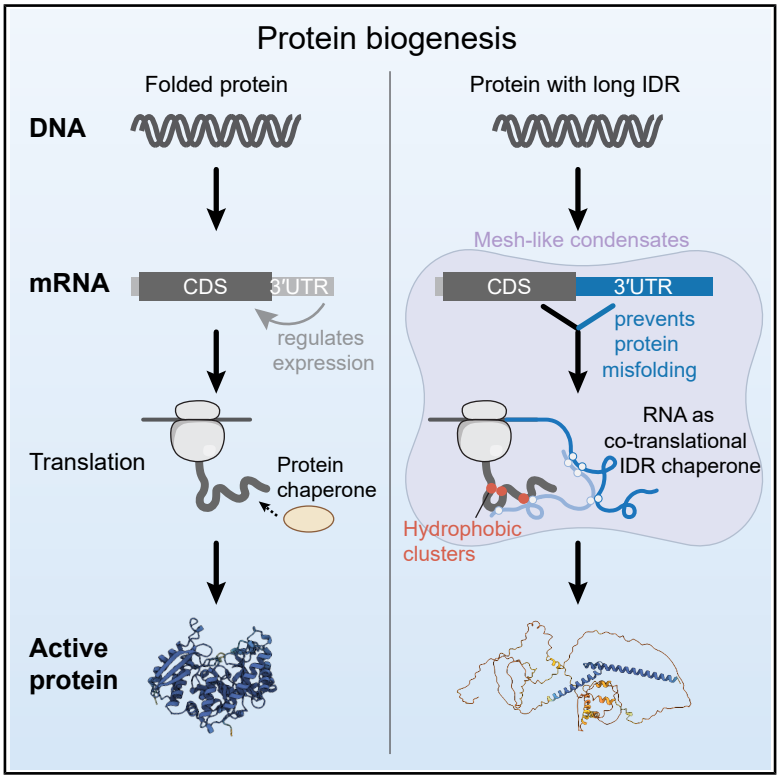

Highlights

- Human mRNAs with highly conserved 3′ UTRs encode proteins enriched for long IDRs
- Highly conserved 3′ UTRs control activity of the mRNA-encoded transcriptional regulators
- 3′ UTRs with IDR chaperone activity are enriched in cytoplasmic mesh-like condensates
- The *KDM6B* 3′ UTR reduces misfolding between IDR hydrophobic clusters and folded domains

Authors

Yang Luo, Yaofeng Zhong, Sudipto Basu, Ming-Chung Wu, Christine Mayr

Correspondence

mayrc@mskcc.org

In brief

Highly conserved mRNA 3′ UTRs act as co-translational chaperones for intrinsically disordered regions (IDRs), preventing inter-domain misfolding and enabling biogenesis of fully active proteins.

Luo et al., 2026, Cell *189*, 4619–4636
July 23, 2026
https://doi.org/10.1016/j.cell.2026.05.017

CellPress

Cell

CellPress

Article

mRNA 3′ UTRs chaperone intrinsically disordered regions to control protein activity

Yang Luo,[1] Yaofeng Zhong,[1,2,3] Sudipto Basu,[1,3] Ming-Chung Wu,[1] and Christine Mayr[1,2,4,*]
[1]Cancer Biology and Genetics Program, Sloan Kettering Institute, New York, NY 10065, USA
[2]Biochemistry, Cell, and Molecular Biology (BCMB) Allied Program, Weill Cornell Graduate School of Medical Sciences, New York, NY 10065, USA
[3]These authors contributed equally
[4]Lead contact
*Correspondence: mayrc@mskcc.org
https://doi.org/10.1016/j.cell.2026.05.017

SUMMARY

More than 2,700 human mRNA 3′ UTRs have hundreds of highly conserved nucleotides, but their biological roles are unclear. These mRNAs encode proteins strongly enriched for long intrinsically disordered regions (IDRs) with hydrophobic amino acid clusters. For MYC, UTX, and JMJD3, we show that their mRNA 3′ UTRs control protein activity. Rather than affecting protein abundance or localization, we find that the *KDM6B* 3′ UTR co-translationally changes the folding of JMJD3 protein. It promotes IDR-IDR interactions and suppresses folding between domains, suggesting that RNA has IDR chaperone activity that prevents interference between hydrophobic clusters in the IDR with folding of the structured domain. 3′ UTRs with chaperone activity are multivalent and mesh-like condensate-enriched, indicating the presence of localized folding environments for IDR-containing proteins. We show here that the protein sequence is insufficient for the biogenesis of fully active IDR-containing transcriptional regulators in cells, suggesting that mRNA 3′ UTRs control their activity by preventing co-translational misfolding.

INTRODUCTION

Messenger RNAs (mRNAs) are central components of gene regulation by providing the templates for protein synthesis. Each mRNA contains a coding sequence (CDS), a 5′ untranslated region (UTR), and a 3′ UTR. Transcriptome-wide mRNA 3′ end sequencing in human primary cells revealed that overall, CDS and 3′ UTRs both contribute nearly 50% of the mRNA sequence.[1,2] Whereas the CDS is translated into the protein sequence, the biological roles of 3′ UTRs are less clear.

Twenty years ago, it was noticed that a subset of human 3′ UTRs has regions with hundreds of nucleotides of exceptionally high sequence conservation, but their functional relevance is unknown.[3] More recently, it was recognized that rapidly evolving 3′ UTRs are GC-rich (high proportion of guanine and cytosine) and repress mRNA and protein expression, whereas conserved 3′ UTRs have a high AU content (percentage of adenine and uracil) and lack repressive functions.[4]

Individual 3′ UTRs have been shown to regulate mRNA stability, mRNA localization, and protein localization.[5–8] However, individual 3′ UTRs often act in a context-specific manner, in which the presence of a regulatory element does not guarantee functional effects.[9,10] Moreover, 3′ UTRs play important roles in cytoplasmic organization, in which they act as scaffolds of mesh-like condensates.[11–14] Importantly, mRNAs do not distribute randomly within the cytoplasm but rather segregate with the help of 3′ UTRs into membrane-associated, condensate-enriched, and unbound cytosolic mRNAs.[13,15–20] In a few cases, the 3′ UTR-determined location of mRNA translation has been shown to control the functions of the newly synthesized proteins.[8,11,21] However, it is currently unclear whether translation of an mRNA in mesh-like condensates versus the cytosol has broader biological consequences.

During protein folding, hydrophobic residues cluster together to form a hydrophobic core, but little is known about the folding of large, multidomain proteins, which usually begins co-translationally.[22–24] Multidomain proteins often contain intrinsically disordered regions (IDRs), which are protein segments with a lower fraction of hydrophobic amino acids than folded domains (FDs).[25] The sequence-structure-function relationships of IDRs remain poorly characterized, as IDRs do not adopt a single stable conformation in isolation but sample a wide array of distinct conformational states.[26,27] As IDRs are strongly enriched in regulatory proteins, including transcription factors and chromatin regulators, a better understanding of how IDRs influence protein function is of broad biological significance.[28]

Here, we show that highly conserved 3′ UTRs in the mRNA templates encoding MYC, UTX, and JMJD3 are required for full transcriptional or histone demethylase activity of the encoded proteins in the nucleus. For cellular JMJD3, protein

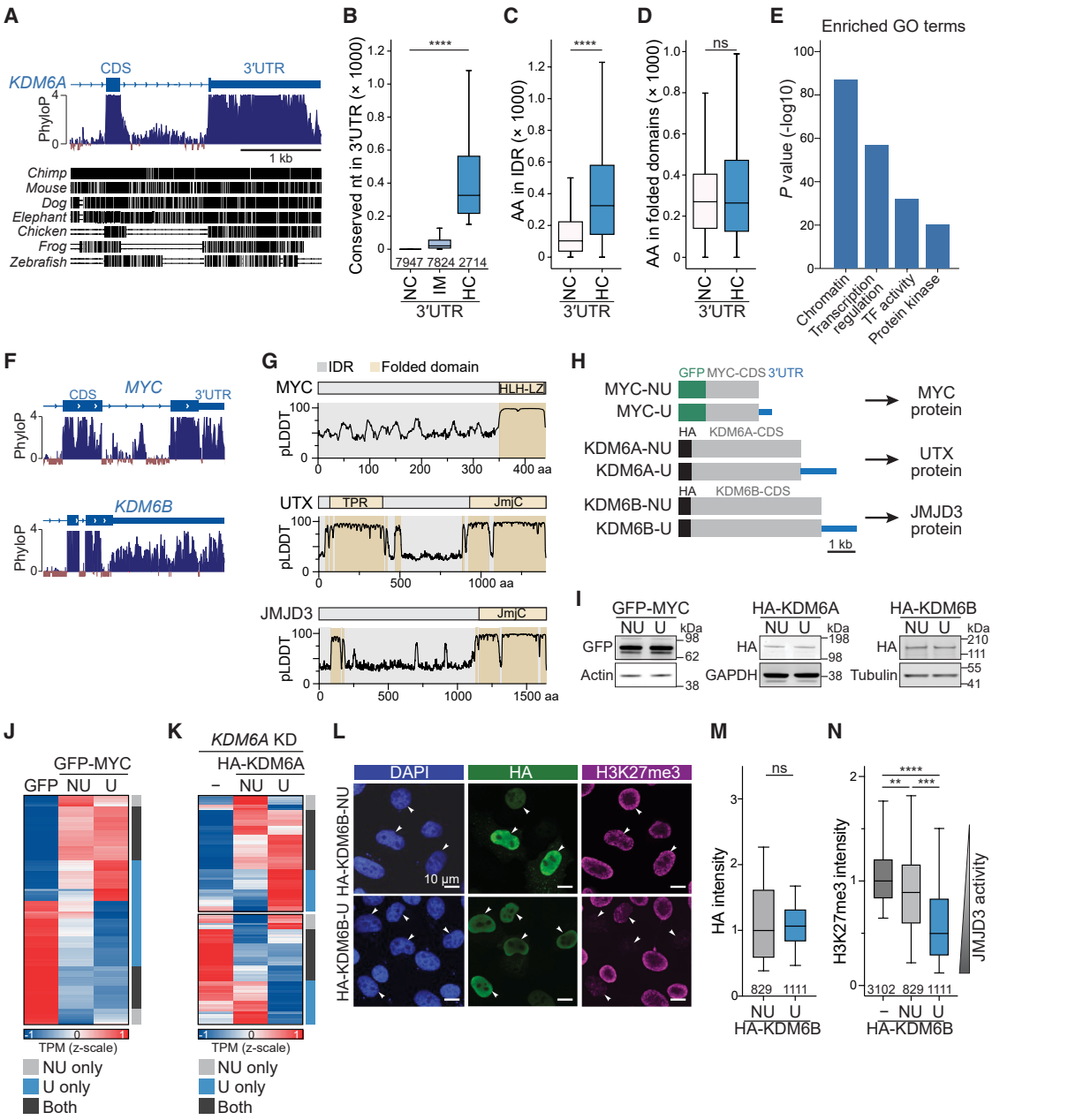

Figure 1. HC 3′ UTRs regulate protein abundance-independent protein activity

(A) UCSC PhyloP100way track shows sequence conservation of 100 vertebrate species for the *KDM6A* gene.

(B) Number of conserved 3′ UTR nucleotides (nt) for three human gene groups. IM, intermediate. Kruskal-Wallis test, $p = 0$.

(C) IDR amino acids (aa) for mRNA-encoded proteins from (B). Mann-Whitney test: $p = 0$.

(D) As in (C), but for folded domains. Folded domain, if IUPreD2A < 0.33. Mann-Whitney test: ns.

(E) Gene ontology analysis showing top categories and Benjamini-Hochberg-adjusted p values of mRNAs with HC 3′ UTRs. TF, transcription factor.

(F) As in (A).

(G) AlphaFold2-predicted folded domains (pLDDT ≥ 80, brown) and IDRs (pLDDT < 80, gray).

(H) cDNA vector constructs showing the tag, CDS (gray), and full-length 3′ UTR (blue). NU, no 3′ UTR; U, 3′ UTR was included.

(I) Western blot after transfection of constructs from (H) into U2OS, MCF7, and HeLa cells. Actin, glyceraldehyde-3-phosphate dehydrogenase (GAPDH), and tubulin serve as loading controls.

(J) Hierarchical clustering of genes with |log2FC| > 0.3 and adjusted p value < 0.1 shows induced (red) or repressed (blue) genes in U2OS cells upon transfection of GFP-MYC-NU or -U compared with GFP. Significant change only in NU versus GFP (NU only; $N = 185$), significant change only in U versus GFP (U only, $N = 753$), and significant change in NU versus GFP and U versus GFP (both, $N = 686$). TPM, transcripts per million.

(legend continued on next page)

activity is controlled by a 3′ UTR-dependent change in protein folding, as shown by crosslinking mass spectrometry. Altered protein folding is recapitulated *in vitro*, in which RNA–IDR interaction is necessary and sufficient for a change in protein domain interaction preference. RNA–IDR binding promotes IDR-IDR interaction and prevents IDR-FD interaction. Our data suggest a model in which the 3′ UTR co-translationally suppresses hydrophobic clusters in the IDR from interfering with the folding of the JMJD3 structured domain. Based on in-cell crosslinking data obtained from ten candidates, we propose that 3′ UTRs have the potential to alter co-translational folding of proteins whose IDRs contain hydrophobic amino acid clusters. For this group, 3′ UTRs in mRNA templates may prevent co-translational misfolding to allow biogenesis of active proteins in cells.

RESULTS

mRNAs with highly conserved 3′ UTRs encode proteins with long IDRs

Previously performed transcriptome-wide mapping of 3′ UTRs revealed that they make up nearly 50% of the human mRNA sequence (Figure S1A).[1,2] Moreover, some 3′ UTRs have regions with strong sequence conservation (Figure 1A). To identify 3′ UTRs with many conserved nucleotides, we used PhyloP conservation scores from 100 vertebrate genomes that include mammals, birds, and fish.[3,29] We define a 3′ UTR as highly conserved (HC) when it has at least 150 nucleotides with PhyloP scores $\geq$2 and only consider regions with at least 4 consecutive nucleotides passing the threshold. Across the entire human genome, only 0.7% of bases meet these criteria, but we detected 2,714 HC 3′ UTRs, 7,947 non-conserved (NC) 3′ UTRs with zero conserved nucleotides, and an intermediate group (Figure 1B; Table S1).

mRNAs with NC 3′ UTRs mostly encode small, well-folded proteins, whereas mRNAs with HC 3′ UTRs encode proteins with long IDRs (Figures 1C and 1D). We define IDRs as protein regions with IUPred2A values $\geq$0.33,[30] but obtained similar results when using AlphaFold-predicted local distance difference test (pLDDT) scores (Figure S1B).[31] Gene ontology analysis showed that mRNAs with HC 3′ UTRs encode proteins substantially enriched in chromatin regulators and transcription factors (Figure 1E),[32] consistent with previous observations that these factors are overrepresented among proteins with long IDRs.[28,33]

HC 3′ UTRs in mRNA templates increase protein activity

To investigate the biological roles of HC 3′ UTRs, we selected three candidate genes (*MYC*, *KDM6A*, and *KDM6B*), whose mRNAs have HC 3′ UTRs and encode proteins with long IDRs (Figures 1A, 1F, and 1G). We used cDNA expression vectors containing the CDS only (called NU, for "no 3′ UTR") or containing CDS and full-length 3′ UTR (called U; Figure 1H) for cellular protein expression. Protein abundance and subcellular localization of the transcriptional regulators were unaffected upon expression from mRNA templates with or without 3′ UTRs (Figures 1I, S1C, and S1D).

Next, we investigated potential differences in protein activity. We expressed MYC-U or MYC-NU in U2OS cells, where endogenous MYC is low, and performed RNA-seq. Compared with the GFP-only control, cells expressing MYC-U induced or repressed nearly twice as many genes as cells expressing MYC-NU (Figure 1J; Table S2). This indicates that inclusion of the 3′ UTR in the mRNA template increases nuclear MYC protein activity in a protein abundance-independent manner.

Similar results were obtained for *KDM6A*, a gene that encodes the H3K27me3 demethylase UTX, which cooperates with transcription and signaling factors to control gene expression programs.[34,35] As UTX is expressed in MCF7 cells (Figure S1E), we knocked down endogenous *KDM6A* and re-expressed hemagglutinin (HA)-tagged UTX protein, followed by RNA-seq. We identified genes that significantly increased or decreased upon *KDM6A* knockdown and whose re-expression of KDM6A-NU or KDM6A-U reversed at least partially the knockdown effect. In cells expressing KDM6A-U, we detected nearly twice as many genes with at least partial rescue of the knockdown effect, compared with cells expressing KDM6A-NU (Figure 1K; Table S2). These data show that the two tested HC 3′ UTRs, when included in mRNA templates, increase the cellular activity of the encoded IDR-containing proteins in a protein abundance-independent manner. These results reveal an unexpected role for protein activity regulation by HC 3′ UTRs.

Two NC 3′ UTRs in mRNA templates do not alter protein activity

We tested whether NC 3′ UTRs in expression vectors also affect protein activity. The *ENO1* gene encodes a glycolytic enzyme called α-enolase, which increases lactate levels in cell culture medium.[36] We knocked down endogenous *ENO1* in HeLa cells, measured the ability of NU and U constructs to rescue lactate production, and did not observe a difference between the two constructs (Figures S1F–S1K). In addition, we tested activity of deoxyhypusine synthase (DHPS). The translation factor EIF5A contains a unique post-translational modification called hypusination. DHPS performs the first step of hypusination, and its activity correlates with EIF5A hypusination level.[37] We knocked down endogenous *DHPS* in HeLa cells, transfected NU and U constructs of DHPS, and did not observe strong differences in EIF5A

(K) As in (J), but shown are MCF7 cells transfected with HA-KDM6A-NU or -U after knockdown (KD) of endogenous *KDM6A*. Hierarchical clustering (separately performed for up- or downregulated groups) if DESeq2 adjusted p value < 0.05. NU only, N = 77; U only, N = 173; both, N = 151.

(L) IF assay for 3′ UTR-dependent cellular JMJD3 activity in HeLa cells after transfection of HA-KDM6B-NU or -U. Nuclei staining by 4′,6-diamidino-2-phenylindole (DAPI). Transfected JMJD3 protein abundance corresponds to anti-HA (green) signal, and the reduction in anti-H3K27me3 staining (magenta) is used to infer JMJD3 activity. White arrowheads mark transfected cells. Representative images are shown.

(M) Quantification of transfected JMJD3 as NU-normalized HA values. Boxplots depict median, 25th and 75th percentiles, and 5%–95% confidence intervals from three independent experiments. Mann-Whitney test: ns.

(N) As in (M), but 3′ UTR-dependent cellular JMJD3 activity is inferred from the reduction in nuclear H3K27me3 intensity in transfected compared with the median intensity in non-transfected cells. Mann-Whitney test, $^{**}p = 6.3 \times 10^{-22}$; $^{***}p = 2.8 \times 10^{-49}$; and $^{****}p = 3.7 \times 10^{-204}$.

hypusination (Figures S1L–S1P). The two NC 3′ UTRs in the mRNA templates did not affect activity of their encoded IDR-lacking proteins.

The *KDM6B* 3′ UTR increases cellular activity of the JMJD3 histone demethylase

Given these results, we set out to study how HC 3′ UTRs—which are not part of proteins—could regulate protein activity. We focused on the *KDM6B* gene, which encodes the JMJD3 H3K27me3 demethylase. We chose it because it allows us to use immunofluorescence (IF) staining to quantify cellular protein abundance and activity in one assay. JMJD3 is expressed at low levels in HeLa cells.[38,39] As a cellular readout for JMJD3 activity, we use a reduction in H3K27me3 levels upon ectopic expression of KDM6B-NU or -U constructs compared with untransfected cells, and we quantify JMJD3 abundance through HA intensity (Figure 1L).

Cells expressing NU or U constructs had comparable HA values, suggesting similar protein levels, which was also observed by western blot analysis (Figures 1I, 1M, S1Q, and S1R). Compared with untransfected cells, we observed a modest reduction in H3K27me3 level with a median decrease of 10% in cells expressing KDM6B-NU. In contrast, we detected a median decrease of over 50% in H3K27me3 staining in cells transfected with KDM6B-U (Figure 1N). This result indicates a substantially higher cellular JMJD3 activity when the protein was translated from the 3′ UTR-containing mRNA template (Figure 1N).

The endogenous *KDM6B* 3′ UTR modulates mesendoderm differentiation

Tightly controlled H3K27me3 levels are crucial during stem cell differentiation and embryonic development.[38] To rule out vector-dependent artifacts, we investigated potential biological effects of the endogenous *KDM6B* 3′ UTR. With CRISPR-Cas9, we deleted 875 base pairs of genomic sequence in human induced pluripotent stem cells (iPSCs). At the mRNA level, this deletion removes 68% of the *KDM6B* 3′ UTR without disrupting the CDS or mRNA 3′ end processing elements (Figures S2A–S2C).

In mouse embryonic stem cells, knockout of *Kdm6b* impairs mesoderm and subsequent cardiomyocyte differentiation.[40] We investigated phenotypic changes during iPSC to mesoderm differentiation upon partial deletion of the *KDM6B* 3′ UTR. In the first three days of cardiomyocyte differentiation in culture, stem cells adopt mesoderm and mesendoderm markers, such as Brachyury, EOMES, and GATA6.[40,41] Deletion of the *KDM6B* 3′ UTR (Udel) did not change endogenous JMJD3 levels, measured by western blot and flow cytometry (Figures S2D and S2E). However, protein abundance of the three tested markers was significantly different in three homozygous Udel clones compared with three clones containing the wild-type 3′ UTR (Figures S2F–S2I). This result suggests that the endogenous *KDM6B* 3′ UTR is important for faithful mesoderm and mesendoderm differentiation. GATA6 is one of the master regulators of heart development,[41] and the strongest 3′ UTR effect was observed for GATA6 (Figures S2H and S2I), suggesting that the *KDM6B* 3′ UTR could play a role during cardiomyocyte differentiation.

The *KDM6B* 3′ UTR is not required for the cellular activity of the IDR-deleted JMJD3 protein

We used the vector constructs to examine the protein-abundance-independent mechanism by which the *KDM6B* 3′ UTR influences JMJD3 activity. Full-length (FL) JMJD3 contains a long N-terminal IDR of over 1,100 residues and a structured C-terminus harboring a JmjC domain with demethylase activity.[38,42] To date, nearly all studies on JMJD3 have used a construct that excludes the N-terminal IDR (IDRdel) and the *KDM6B* 3′ UTR (Figures 2A and 2B).[38,42–45]

Protein abundance of the FL and IDR deletion constructs was similar, as determined by HA intensity (Figures 2C and 2D). Expression of only the FD generates an active JMJD3 protein. It reduces H3K27me3 staining by 50%, comparable to the reduction observed with the U construct (Figure 2E). Moreover, the *KDM6B* 3′ UTR is not required for biogenesis of an active protein that contains the FD only (Figures 2C–2E). This experiment demonstrates a functional link between the JMJD3 IDR in the protein and the *KDM6B* 3′ UTR in the mRNA: when both components are present, or when both are absent, a fully active protein is generated. Without the mRNA 3′ UTR, the IDR negatively affects JMJD3 protein activity, but the repressive effect of the IDR is overcome by the 3′ UTR in the native mRNA.

The *KDM6B* 3′ UTR does not control chromatin localization of JMJD3

Protein localization can regulate protein activity.[6–8] It is possible that the *KDM6B* 3′ UTR controls JMJD3 subnuclear localization and, subsequently, its activity. We expressed the HA-tagged constructs and used chromatin immunoprecipitation and sequencing (ChIP-seq) as a high-resolution readout for JMJD3 protein localization. HA signal quantification showed reduced chromatin occupancy of the IDR-deleted compared with the FL protein (Figures S3A and S3B). Importantly, subnuclear localization of FL JMJD3 was not affected by the *KDM6B* 3′ UTR (Figures S3A and S3B), demonstrating that JMJD3 protein localization is 3′ UTR-independent.

In parallel, we performed H3K27me3 ChIP-seq to investigate the effects of IDR and mRNA 3′ UTR on genome-wide cellular activity of JMJD3 (Figures S3C and S3D). ChIP-seq confirmed the IF results: IDR deletion or expression of the U construct strongly reduced the H3K27me3 signal, consistent with full cellular JMJD3 activity (Figures S3C and S3D). In contrast, expression of the FL protein from the NU vector only showed partial protein activity, as the reduction in methylation was 50% compared with the U construct (Figures S3C and S3D).

Protein activity can also be regulated by protein interactors, post-translational modifications, or directly through protein conformation.[46] We expressed JMJD3 from NU or U constructs and performed SILAC-based JMJD3 immunoprecipitation followed by mass spectrometry. We did not observe major differences in 3′ UTR-dependent protein interactors or modifications (Figures S3E–S3I; Table S3). Therefore, we hypothesized that the *KDM6B* 3′ UTR alters JMJD3 protein conformation directly.

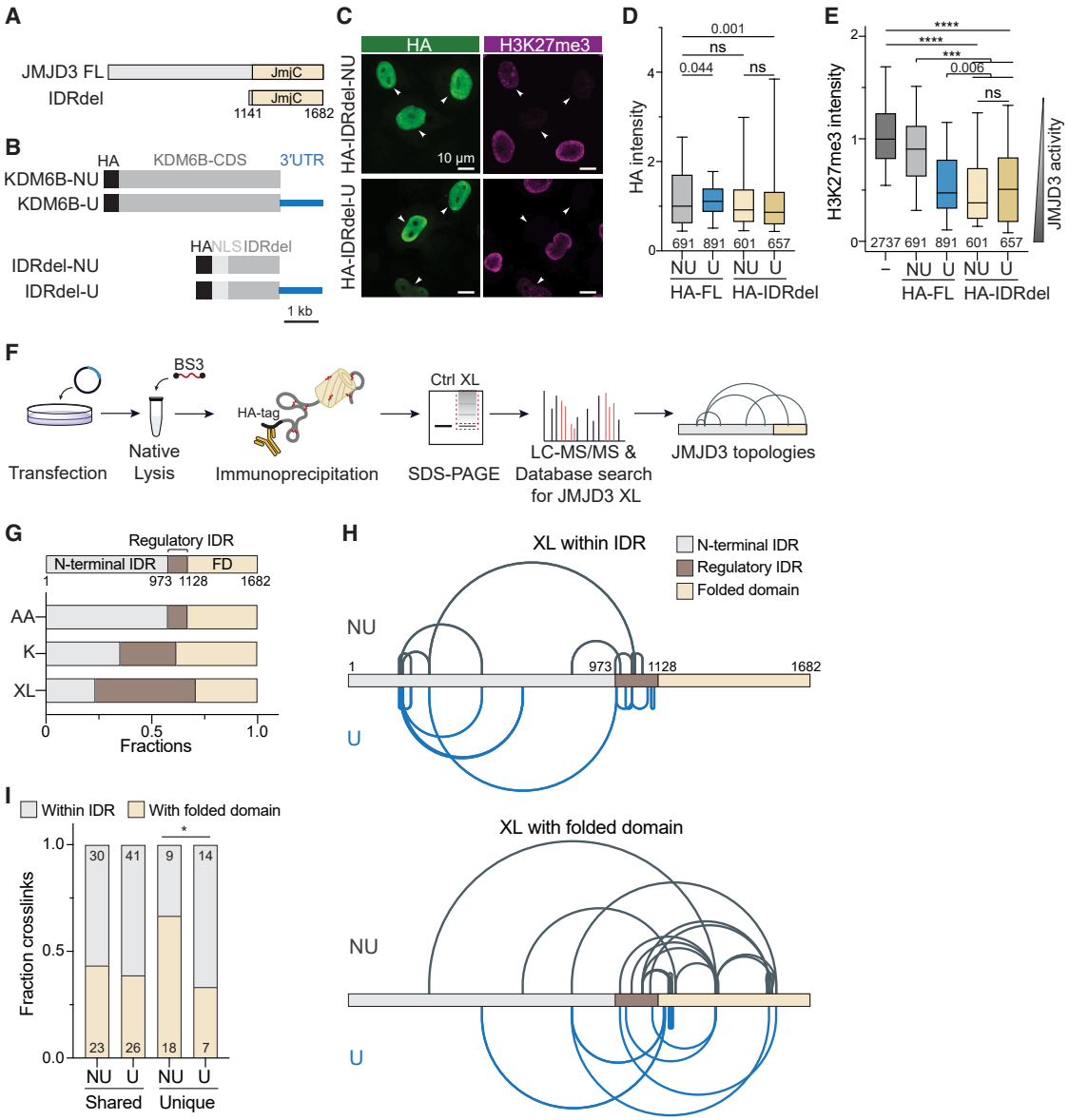

Figure 2. 3′ UTR-dependent protein conformation and activity depend on the JMJD3 IDR

(A) Full-length (FL) and IDR-deleted (IDRdel) JMJD3 protein models. Yellow, JmjC domain; IDR, gray; numbers, aa boundaries.

(B) As in Figure 1H. NLS, nuclear localization signal.

(C) As in Figure 1L, using constructs from (B).

(D) As in Figure 1M using constructs from (B). Mann-Whitney test.

(E) As in Figure 1N using constructs from (B). Mann-Whitney test. ***$p = 7.8 \times 10^{-80}$; ****$p < 10^{-139}$.

(F) XL-MS workflow to examine cellular JMJD3 conformation.

(G) Fraction of aa, lysines (K), and XL mapping to the indicated JMJD3 regions. FD, folded domain.

(H) XL depicted as lines connecting the crosslinked residues. Shown are unique XL detected after JMJD3 expression from NU (gray) or U (blue) constructs.

(I) Quantification of XL from (H), also shown are XL detected in both NU and U samples (shared). Test for independent proportions, $p = 0.02$.

The *KDM6B* 3′ UTR in the mRNA template changes steady-state JMJD3 protein conformation

To test this hypothesis, we expressed JMJD3 in cells from NU or U constructs, followed by BS3 (bis(sulfosuccinimidyl)suberate)-mediated crosslinking mass spectrometry (XL-MS; Figure 2F). We focused on JMJD3 crosslinks to assess protein conformation. As quality controls, we determined frequencies of looplinks, monolinks, and crosslinks and did not observe significant differences between NU and U samples (Table S3), consistent with similar crosslinking efficiency. Interestingly, we observed that most IDR crosslinks mapped to a small region located upstream of the C-terminal FD, which we call "regulatory IDR," as it only covers 9% of the sequence but contains 47% of crosslinks (Figure 2G).

Next, we analyzed the unique crosslinks detected in either NU or U samples and observed a significant, 3′ UTR-dependent difference in crosslinking pattern (Figures 2H and 2I; Table S3). When generating JMJD3 from a 3′ UTR-containing mRNA template, two-thirds of unique crosslinks are indicative of IDR-IDR interactions, whereas two-thirds of unique crosslinks are involved in binding to the FD when the 3′ UTR is lacking (Figure 2I). This experiment provides direct evidence for a 3′ UTR effect on JMJD3 protein conformation involving its IDR. It suggests that the *KDM6B* 3′ UTR promotes interactions within the IDR, whereas its absence induces protein folding across domains, that is, between the IDR and the FD.

A hydrophobic segment in the IDR represses JMJD3 activity

To learn how the mRNA 3′ UTR changes IDR-dependent protein conformations, we determined the regulatory logic of the IDR. Examination of the amino acid composition of the IDR regulatory domain revealed two regions: a positively charged stretch with +18 net charge and a small highly hydrophobic (HP) region (Figures 3A and S3J). The HP region is largely conserved across vertebrates and has the highest sequence conservation within the entire IDR (Figure 3A). Deletion of the HP region strongly decreased H3K27me3 staining, thus increasing JMJD3 activity, even when expressed from an mRNA template lacking the 3′ UTR (Figures 3B, 3C, and S3K). This result indicates that the HP segment in the IDR substantially represses cellular JMJD3 activity when the protein is translated from a 3′ UTR-lacking mRNA.

The RNA-binding region in the IDR mediates the 3′ UTR effect on JMJD3 protein activity

Positively charged IDR regions were previously reported to act as RNA-binding regions (RBRs).[47,48] To examine whether the positively charged IDR segment acts as RBR in cells, we deleted it and performed infrared individual-nucleotide resolution crosslinking and immunoprecipitation (irCLIP) (Figures 3A and 3D).[49,50] Compared with the FL JMJD3 protein, RBR deletion strongly reduced the RNA signal, showing that it is the major RNA-binding region (Figure 3E). Moreover, deletion of the RBR strongly reduced activity of JMJD3 generated from a 3′ UTR-containing mRNA template, as it only weakly decreased H3K27me3 staining (Figures 3F, 3G, and S3L). This result indicates that the RBR in the JMJD3 IDR mediates the 3′ UTR effect on cellular protein activity.

Although the RBR is necessary, it is not sufficient for JMJD3 activity. Both versions of FL JMJD3 protein—generated from NU or U constructs—contain this region, but only the protein generated from the U construct shows full activity. As both protein versions bind to RNA in cells, we infer that there must be a difference between post-translational and co-translational RNA binding. In our working model, the 3′ UTR in the mRNA template allows co-translational interaction between the 3′ UTR and the IDR in the nascent chain, thus being capable of directly changing JMJD3's protein conformation. The co-translational conformation cannot be reversed by post-translational RNA binding (Figure 3H).

RNA-IDR binding changes JMJD3 domain interaction preference *in vitro*

To examine whether RNA can directly change protein conformation, we used recombinant JMJD3 protein domains and assessed RNA-dependent interactions. We focused on the regulatory IDR and FD, as these regions predominantly interacted according to XL-MS (Figures 2H and 2I). We used *in vitro* protein crosslinking to test whether *in vitro* transcribed RNA changes the frequency of IDR-IDR and IDR-FD interactions.

The regulatory IDR and the C-terminal FD were generated as separate protein domains (Figures 4A and S4A). *In vitro* RNA binding of the two domains was assessed through fluorescence polarization assays. At the tested concentrations, we observed no RNA binding to the FD, but strong binding to the regulatory IDR at physiological salt concentration (Figures S4B–S4D), which required the RBR (Figure S4E). The RBR has a high positive net charge but lacks known RNA-binding motifs (Figure S4F). As the IDR binds with similar affinity to different *in vitro* transcribed RNAs, the RNA–IDR interactions seem to be electrostatic and not sequence specific (Figures S4B–S4E).

To test changes in protein domain interactions caused by RNA binding, we performed a bismaleimidoethane (BMOE)-mediated thiol-thiol crosslinking assay (Figure 4B). We used native cysteines in the FD, mutated all three cysteines in the regulatory IDR, and introduced a single cysteine into the HP region (Figure 4A). The FD did not form a crosslinked product, and addition of different RNAs (*KDM6B or HSPA1B* 3′ UTRs) had no effect, consistent with its inability to bind RNA (Figures 4B [lanes 4 and 6] and S4G).

In the absence of RNA, mixing of FD and regulatory IDR generated near equal amounts of IDR-IDR and IDR-FD dimers (Figures 4B [lane 7] and S4G). Addition of RNA to the mixture strongly promoted IDR-IDR interaction, resulting in a 95:5 dimer ratio (Figures 4B [lane 8] and S4G). The interaction pattern observed with recombinant protein domains perfectly mimics the domain interactions observed by XL-MS obtained from cells at steady-state levels, where FL JMJD3 was generated from an mRNA with or without 3′ UTR (Figures 2H and 2I).

In contrast, absence of the RBR in the IDR abrogated the RNA-mediated increase in IDR-IDR interactions (Figures 4C and S4H), indicating that both the RNA and the RNA-binding region need to be present simultaneously for the switch in domain interaction preference toward IDR-IDR interactions. This experiment demonstrates that RNA–IDR binding is necessary and sufficient for the change in domain interaction preference between the JMJD3 IDR and its FD *in vitro*. The *in vitro* crosslinking experiment fully recapitulated the 3′ UTR-dependent increase in IDR-IDR interaction at the expense of IDR-FD interaction observed by XL-MS. These results strongly suggest that JMJD3 conformations are changed by 3′ UTR-provided chaperone activity.

Co-translational changes in JMJD3 nascent chain conformation require cooperation of 3′ UTR and IDR RBR

Next, we investigated whether the *KDM6B* 3′ UTR has the capacity to alter cellular JMJD3 nascent chain conformations. AlphaFold3 predicts that JMJD3 forms a domain-swapped dimer, in which the HP region binds to the FD of another

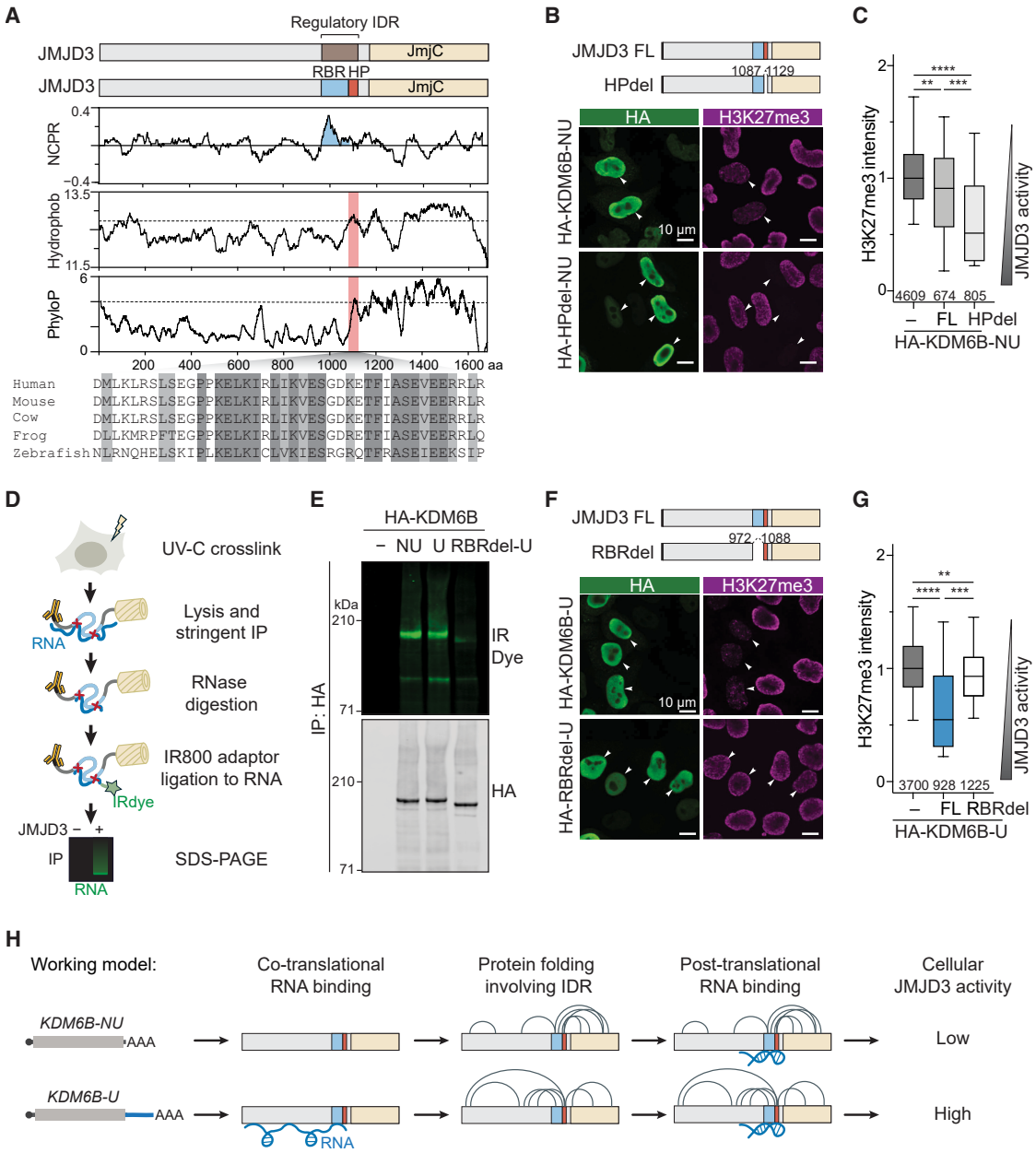

Figure 3. The JMJD3 IDR contains segments with opposing effects on protein activity

(A) The regulatory IDR contains a putative RNA-binding region (RBR, aa 973–1087, blue) and a conserved hydrophobic region (HP, aa 1088–1128, red). Top: net charge per residue (NCPR). Middle: hydrophobic scale values per residue. Bottom: 100-way PhyloP scores of KDM6B CDS. Below: HP region aa alignment across species. Dark gray, perfect conservation; light gray, conservative substitution.

(B) As in Figure 1L, but indicated constructs were used.

(C) As in Figure 1N for constructs from (B). Mann-Whitney test: $^{**}p = 2.8 \times 10^{-17}$; $^{***}p = 5.0 \times 10^{-23}$; and $^{****}p = 3.1 \times 10^{-133}$.

(D) irCLIP workflow to detect cellular RNA-JMJD3 binding.

(E) irCLIP of indicated constructs expressed in HeLa cells.

(F) As in Figure 1L, but indicated constructs were used.

(G) As in Figure 1N for constructs from (F). Mann-Whitney test: $^{**}p = 5.5 \times 10^{-17}$; $^{***}p = 2.6 \times 10^{-77}$; and $^{****}p = 1.4 \times 10^{-137}$.

(H) Working model for differential effect of co- and post-translational RNA–IDR interaction during 3′ UTR-dependent regulation of cellular JMJD3 activity.

JMJD3 molecule (Figure S4I).[51,52] Domain-swapped dimers are often generated through co-translational protein complex assembly.[53–55]

We developed a disome assay to investigate whether the *KDM6B* 3′ UTR changes JMJD3 protein conformation co-translationally (Figure 4D). Disomes are stable pairs of ribosomes

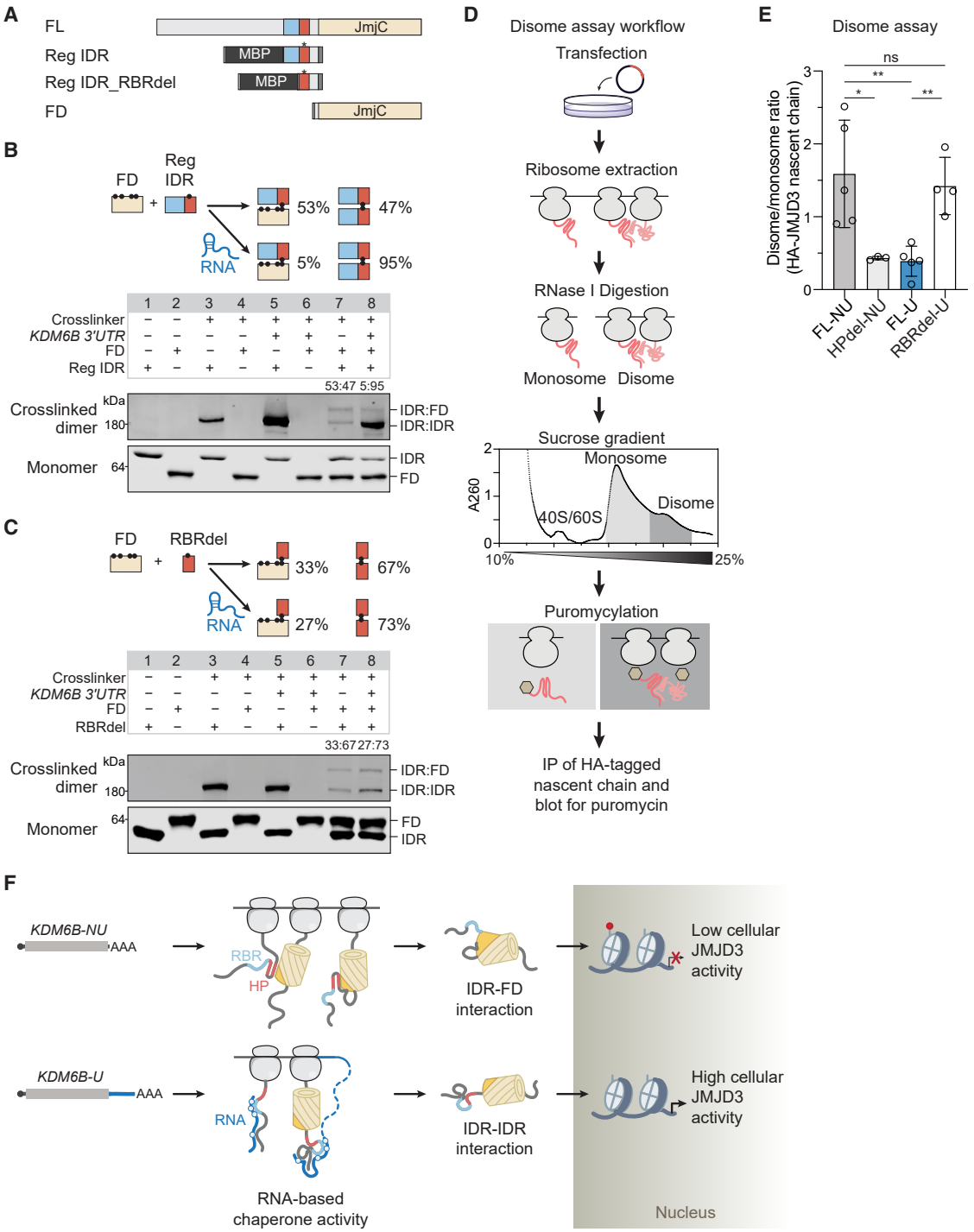

Figure 4. RNA-IDR interaction is necessary and sufficient for changing JMJD3 domain interaction preference

(A) JMJD3 constructs for *in vitro* assays. All contain N-terminal 6×His-tag (medium gray) and C-terminal Strep-tag (dark gray). Introduction of cysteine (E1102C; asterisk) for crosslinking.

(B) BMOE-mediated thiol-thiol crosslinking immunoblots showing RNA-dependent protein-protein interactions between recombinant JMJD3 regulatory (reg) IDR and folded domain (FD). Two gels are used to resolve the dimer and monomer bands. Figure S4G shows the same reactions loaded onto one gel.

(C) As in (B) but for RBRdel instead of reg IDR. Full gel in Figure S4H.

(legend continued on next page)

isolated from cells through RNase digestion and sucrose gradient centrifugation. Disomes either form through stress-associated ribosome collisions or occur physiologically, through stable nascent chain interaction from neighboring ribosomes.[54,56,57] We transfected our constructs, extracted monosomes and disomes from cells, used puromycin to label nascent chains in each fraction, and immunoprecipitated JMJD3 nascent chains with HA antibody, followed by normalization to the ribosomal protein RPLP0, to adjust for differences in input (Figure S4J). We ruled out stress-associated ribosome collisions, as we did not observe differences in ZAK phosphorylation (Figures S4K and S4L).[56]

The presence of JMJD3 in disomes indicates co-translational homodimerization, whereas its presence in monosomes indicates a monomeric protein.[54,55] We quantified JMJD3 nascent chains in disomes versus monosomes and inferred co-translational differences in protein conformation through changes in disome-over-monosome ratios. Whereas FL JMJD3 translated from the NU construct prefers disomes, translating it from the U construct prefers monosomes (Figure 4E), thus demonstrating a co-translational effect of the mRNA 3′ UTR on JMJD3 conformation.

To test whether the regulatory IDR is involved in the co-translational JMJD3-nascent chain interactions, we examined the HP and RBR deletion constructs. Whereas the HP region increases JMJD3's presence in disomes, the RBR decreases it (Figure 4E). These results show that the 3′ UTR in the native mRNA and the RBR in the IDR cooperate to avoid the co-translational nascent chain conformations induced by the HP region in the NU-translated protein (Figure 4E).

These results are consistent with a model (Figure 4F), in which the 3′ UTR co-translationally binds to the IDR and directly changes domain interaction preference. In the absence of the 3′ UTR, the HP segment in the IDR may cause co-translational misfolding of the structured domain, thus permanently reducing JMJD3 protein activity. The co-translational misfolding is prevented by the *KDM6B* 3′ UTR in the mRNA, suggesting that it has IDR chaperone activity during protein folding.

Not all 3′ UTRs have JMJD3 IDR chaperone activity

Our *in vitro* assays suggest an electrostatic RNA–IDR interaction that induces a sequence-independent change in JMJD3 domain interaction preference (Figures S4D–S4H). Therefore, we investigated whether other 3′ UTRs have JMJD3 IDR chaperone activity in cells. In the KDM6B-U vector, we swapped the *KDM6B* 3′ UTR with four different 3′ UTRs and tested JMJD3 activity (Figure 5A). For two 3′ UTRs, derived from *IDH1* or *HSPA1B* mRNA, H3K27me3 staining was substantially reduced, consistent with IDR chaperone activity, whereas the other two behaved like the NU construct, suggesting an absence of chaperone activity (Figures 5A, 5B, S5A, and S5B).

HC 3′ UTRs are multivalent and strongly enriched in mesh-like condensates

To identify RNA features that distinguish 3′ UTRs with or without IDR chaperone activity, we compared HC and NC 3′ UTRs. They differ substantially with respect to enriched 6-mer motifs, 3′ UTR length, AU content, mean free energy of their predicted secondary structures, and RNA–RNA binding site density (Figures S5C–S5I; Table S1).[4] These features correlate with each other and are associated with multivalent RNAs (Table S4).[12]

RNA valency describes accessible RNA–RNA interaction sites.[12] Multivalent RNAs were previously shown to generate mesh-like condensates *in vitro* and *in vivo* by acting as condensate scaffolds.[12] RNA valency is determined by both RNA length and structure.[12,58,59] To predict RNA valency of cellular mRNAs, we identified a surrogate marker for multivalent 3′ UTRs: the sum of A or U homopolymers with at least five consecutive nucleotides, called A5/U5, correlates strongly with both RNA length and weak predicted RNA structure and combines the two essential features of multivalent RNAs (Table S4). Moreover, A5/U5 separates the two groups of RNAs initially used to distinguish multivalent and low-valency RNAs experimentally (Figure S5J).[12] Going forward, we are using A5/U5 as proxy for 3′ UTR valency.

High A5/U5 is strongly associated with cellular mRNAs enriched in mesh-like condensates, whereas low A5/U5 characterizes cytosol-localized mRNAs (Figure 5C).[13,14] Moreover, A5/U5 separates perfectly HC from NC 3′ UTRs (Figure 5D). Intersection of HC 3′ UTRs with mesh-like condensate-enriched mRNAs revealed a very strong overlap, as 91% of HC 3′ UTRs are condensate-enriched (Figure 5E). Our data suggest that HC 3′ UTRs are multivalent, allowing the 3′ UTR-containing mRNAs to localize and become entrapped in cellular mesh-like condensates (Figure 5F). In contrast, mRNAs with NC 3′ UTRs have low valency, which prevents their capture by mesh-like condensates and promotes their cytosolic localization.[12]

The tested multivalent 3′ UTRs have JMJD3 IDR chaperone activity

A5/U5 distinguishes 3′ UTRs perfectly with or without JMJD3 IDR chaperone activity: 3′ UTRs that increased cellular JMJD3 protein activity had multivalent 3′ UTRs, containing seven to 21 A/U homopolymers. In contrast, 3′ UTRs without chaperone activity had low-valency 3′ UTRs, containing zero or one A/U homopolymer (Figure 5G).

To validate that A5/U5 in 3′ UTRs predicts mRNA enrichment in cellular mesh-like condensates, we performed a previously established "digitonin RNA-fluorescence *in situ* hybridization (FISH)." Digitonin extracts cytosolic mRNAs and retains cellular mesh-like condensate-enriched mRNAs.[13] 3′ UTR-containing *MYC*, *KDM6A*, and *KDM6B* mRNAs have at least two-fold higher A5/U5 values compared with their 3′

(D) Workflow of disome assay. HeLa cells transfected with the indicated constructs were lysed, ribonuclease-treated, separated into monosome/disome fractions, and nascent chains labeled with puromycin (hexagon). HA-immunoprecipitated, newly synthesized protein was detected by anti-puromycin immunoblot, normalized to input RPLP0.

(E) Experiment from (D) shown as mean ± SD from five independent experiments. Raw data shown in Figure S4J. Unpaired *t* test: $*p < 0.05$; $**p < 0.01$.

(F) Model for the *KDM6B* 3′ UTR acting as a co-translational IDR chaperone during protein folding, thus causing differences in cellular JMJD3 activity.

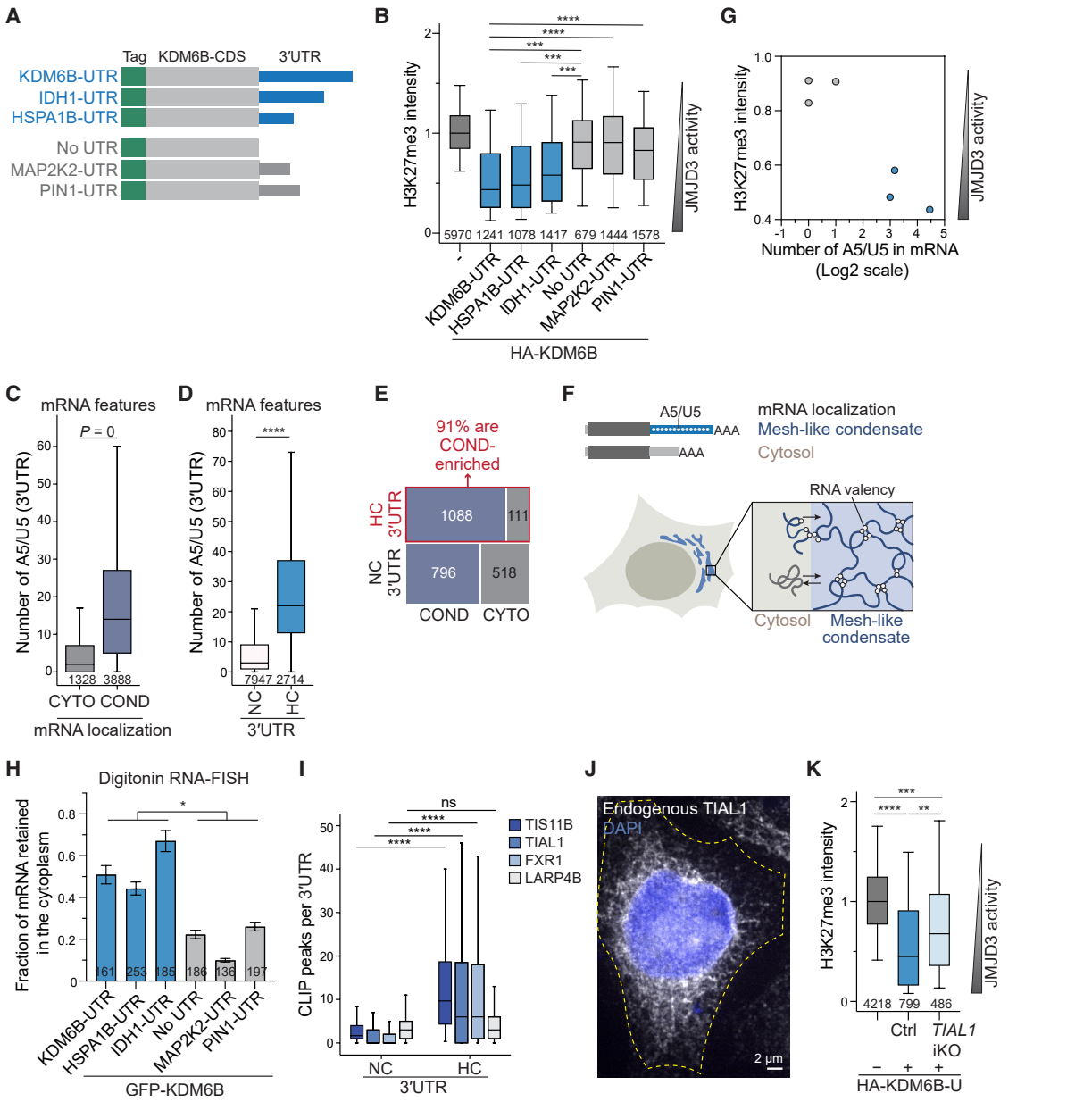

Figure 5. 3′ UTRs with chaperone activity are multivalent and enriched in mesh-like condensates

(A) Constructs for 3′ UTR-swapping experiments. The KDM6B CDS was fused with four different 3′ UTRs. Blue, 3′ UTRs with IDR chaperone activity; gray, 3′ UTRs without IDR chaperone activity.

(B) As in Figure 1N, but for constructs from (A). Mann-Whitney test, $^{***}p < 10^{-39}$; $^{****}p < 10^{-84}$.

(C) Number of A/U homopolymers (A5/U5) as a surrogate marker of RNA valency for cytosol-enriched (cyto) or mesh-like condensate-enriched (cond) mRNAs. Mann-Whitney test, 8.4×10^{-182}.

(D) As in (C) but for HC and NC 3′ UTRs. Mann-Whitney, $p = 0$.

(E) Contingency table for mRNAs with HC or NC 3′ UTRs and their subcytoplasmic localization as in (C). $\chi^2 = 302.38$, $p < 0.0001$.

(F) Model for entrapment of mRNAs with multivalent 3′ UTRs (white dots on blue) through RNA-RNA interactions in cytoplasmic mesh-like condensates. mRNAs with low-valency 3′ UTRs (gray) are not entrapped and mostly localize to the cytosol.

(G) Relationship between mRNA multivalency and 3′ UTR-dependent cellular JMJD3 activity from (B).

(H) Digitonin RNA-FISH of constructs from (A) in HeLa cells. Shown is RNA-FISH signal after digitonin treatment as mean ± SEM from three independent experiments. *N*, analyzed cells. *t* test for independent samples, $^{*}p = 0.014$.

(I) 3′ UTR CLIP peaks of condensate-enriched RNA-binding proteins. LARP4B is not condensate enriched and serves as a negative control. Mann-Whitney test, $^{****}p < 10^{-243}$.

(J) IF of endogenous TIAL1 in HeLa cells. DAPI stains the nucleus. Cell boundary (yellow dotted line). A representative image is shown.

(K) As in Figure 1N, but for the indicated conditions. $^{**}p = 1.4 \times 10^{-13}$; $^{***}p = 5.7 \times 10^{-40}$; and $^{****}p = 3.0 \times 10^{-130}$.

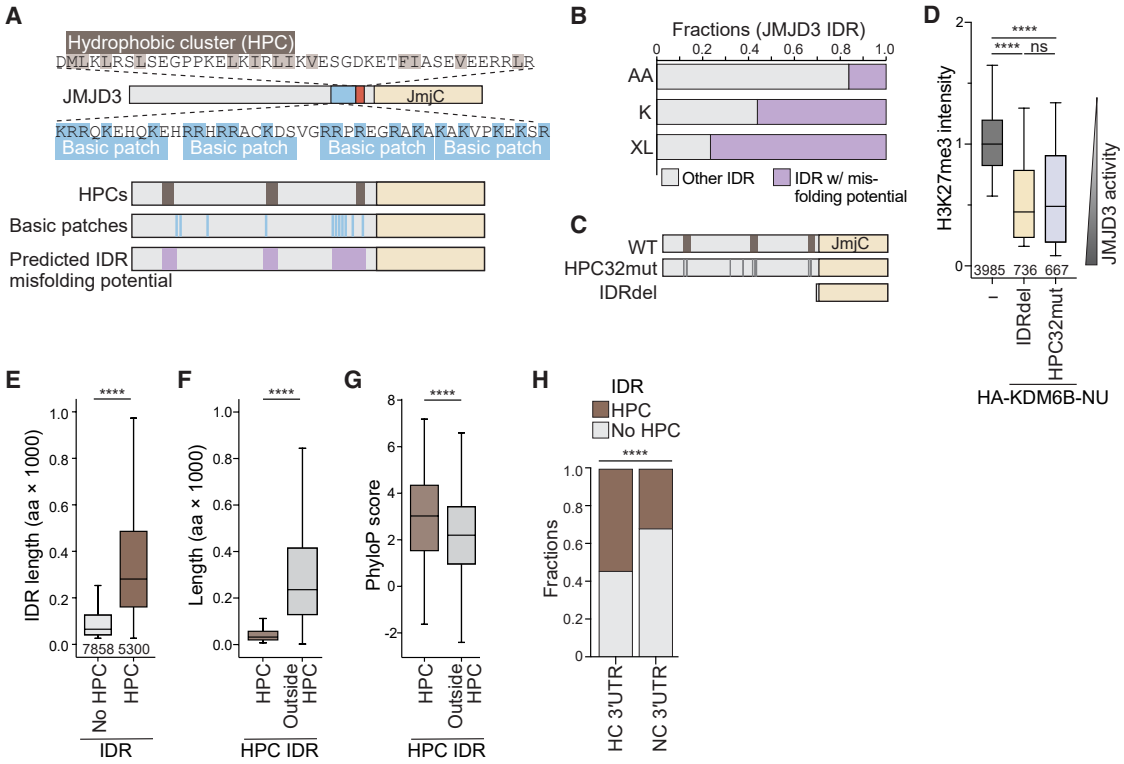

Figure 6. IDR HPCs participate in JMJD3 protein folding

(A) Mapping of HPCs and basic patches in the JMJD3 IDR.

(B) As in Figure 2G, but for regions shown in (A).

(C) Mutation of 32 hydrophobic residues within IDR HPCs (HPC32mut)

(D) As in Figure 1N, but for the constructs from (C). Mann-Whitney test: ****$p < 10^{-131}$.

(E) IDR length distribution of the longest IDR of IDR-containing proteins. Brown, HPC IDRs; gray, IDRs lacking HPCs. Mann-Whitney test: ****$p = 0$.

(F) Length of HPC and surrounding IDR for HPC-containing IDRs. Wilcoxon test: ****$p = 0$.

(G) As in (F), but 100-way PhyloP scores of the indicated regions. Wilcoxon test: $p = 1.7 \times 10^{-310}$.

(H) HPC IDRs versus IDRs lacking HPCs for mRNAs with HC ($N = 2,354$) or NC 3′ UTRs ($N = 4,703$). Chi-square test, $\chi^2 = 310$, ****$p < 0.00001$.

UTR-deleted counterparts. In digitonin-treated RNA-FISH, the 3′ UTR-containing mRNAs were significantly more retained in the cytoplasm than their 3′ UTR-deleted counterparts (Figures S6A–S6C).

A similar cytoplasmic retention pattern was observed for multivalent 3′ UTRs with IDR chaperone activity. Although these 3′ UTRs were not conserved, mRNAs with the *IDH1* or *HSPA1B* 3′ UTR were significantly more retained in digitonin-treated cells than mRNAs with 3′ UTRs lacking chaperone activity (Figures 5H and S6D). Taken together, for eight tested 3′ UTRs, we observed a strong correlation between 3′ UTR A5/U5 content, enrichment in cytoplasmic mesh-like condensates, and RNA-mediated chaperone activity (Figures 5C–5H and S6A–S6D), suggesting that mesh-like condensates represent subcellular compartments with IDR chaperone activity.

JMJD3 IDR chaperone activity requires TIAL1, a mesh-like condensate-enriched RNA-binding protein

Mesh-like condensates contain multivalent mRNAs and specific RNA-binding proteins.[11–14] To strengthen the link between mesh-like condensates and IDR chaperone activity, we investigated whether TIS11B, TIAL1, or FXR1, which represent mesh-like condensate-enriched RNA-binding proteins,[13,14] contribute to chaperone activity. Quantification of 3′ UTR-mapped CLIP peaks of these RNA-binding proteins revealed that HC 3′ UTRs contain significantly more peaks than NC 3′ UTRs. LARP4B is not enriched in mesh-like condensates and serves as a negative control (Figure 5I).[13]

The *KDM6B* 3′ UTR is a strong TIAL1 CLIP target (Table S1).[60] Staining of endogenous TIAL1 in HeLa cells shows a reticulated, perinuclear localization pattern and supports TIAL1 enrichment in mesh-like condensates (Figure 5J).[13] We investigated whether TIAL1 is necessary for IDR chaperone of the *KDM6B* 3′ UTR. When JMJD3 was generated from the U construct in cells lacking TIAL1, we observed a lower reduction of H3K27me3 levels compared with TIAL1-containing control cells (Figure 5K). This result shows that the condensate-enriched RNA-binding protein TIAL1 is required for full chaperone activity of the *KDM6B* 3′ UTR (Figures 5K and S6E–S6G) and is consistent with a model by which multivalent 3′ UTRs within mesh-like condensates act as IDR chaperones.

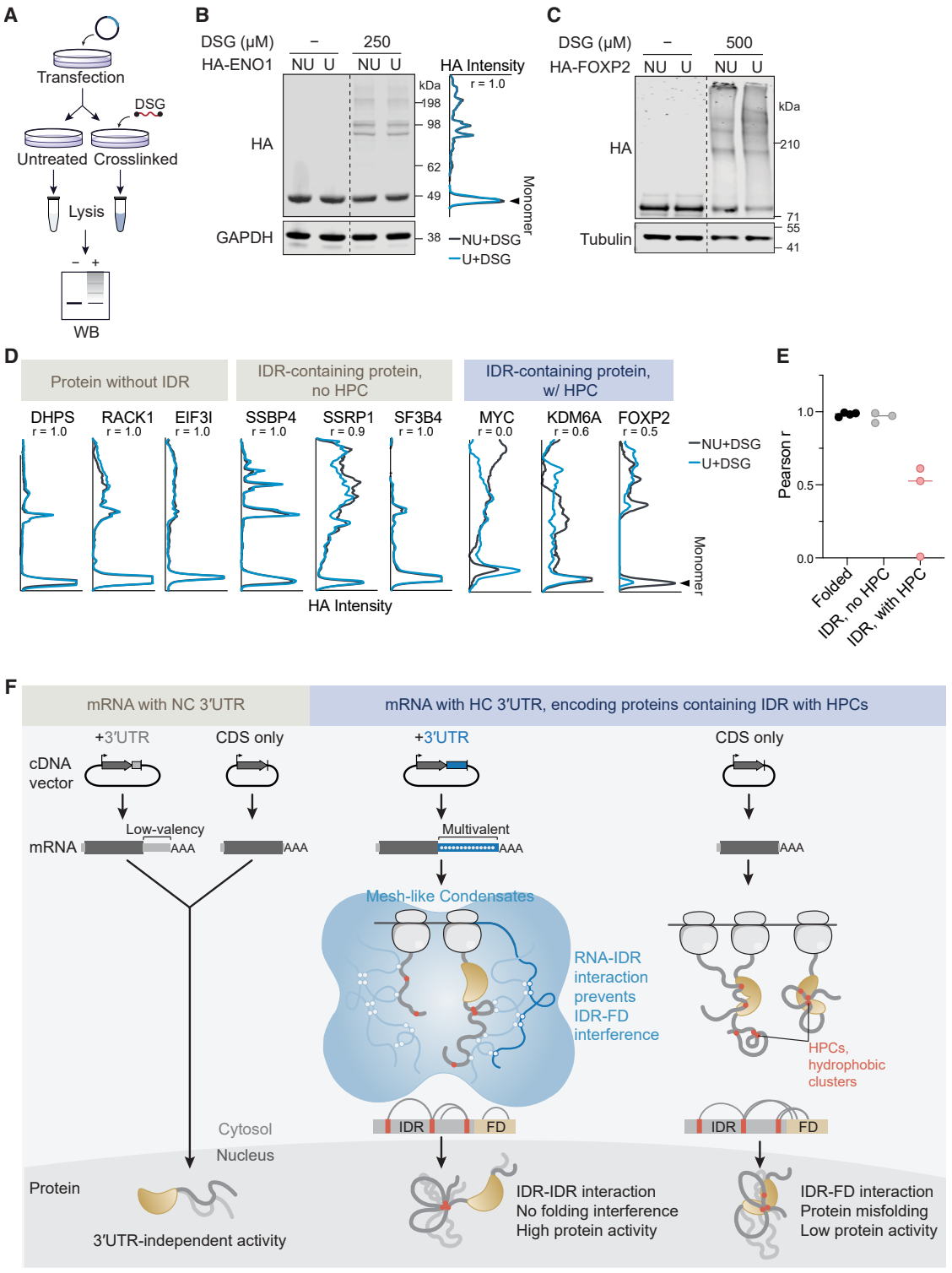

Figure 7. 3′ UTR-dependent protein states of HPC IDR-containing proteins

(A) Workflow for DSG chemical crosslinking in cells, followed by western blot.

(B) Western blot of HeLa cells transfected with HA-ENO1-NU or -U for non-crosslinked and DSG-crosslinked conditions. Dotted lines indicate removal of irrelevant lanes. Line profiles and corresponding Pearson's correlation coefficient quantify 3′ UTR-dependent differences in protein crosslinking patterns.

(legend continued on next page)

Hydrophobic amino acid clusters in the JMJD3 IDR have misfolding potential

Lastly, we investigated the JMJD3 IDR features that require RNA-mediated chaperone activity. The IDR regulatory region contains several basic patches, followed by a short region with clustered hydrophobic amino acids (hydrophobic cluster, HPC) (Figure 6A). In the JMJD3 IDR, we observed two more regions with basic patches adjacent to HPCs (Figure 6A). Intersection of the combined basic/HPC regions with the XL-MS data revealed that these regions harbor 77% of IDR crosslinks but only represent 16% of the IDR sequence (Figure 6B), suggesting that these IDR regions participate in protein folding, potentially causing misfolding in the absence of the mRNA 3′ UTR.

We tested this hypothesis. The entire JMJD3 IDR contains 210 hydrophobic residues, 32 of which are located within the HPCs. Notably, expression of the HPC32mut construct generated an active JMJD3 protein in the absence of the 3′ UTR, with cellular activity being equal to deletion of the entire IDR (Figures 6C, 6D, S7A, and S7B). Although the protein generated from the HPC32mut construct contains more than 1,100 IDR residues, there is no evidence for IDR-mediated protein misfolding in the absence of the 3′ UTR. This result supports a model in which IDR HPCs cause misfolding of the structured domain during co-translational JMJD3 protein folding if not prevented by chaperone activity of condensate-enriched 3′ UTRs.

Local IDR sequence conservation in HPCs

In the human proteome, we identified 5,300 HPC-containing IDRs (Table S1). This corresponds to 40% of tested IDRs when focusing on the longest IDR of each protein. HPC-containing IDRs are long, having a median length of 277 amino acids (Figure 6E). HPCs are small and represent approximately 11% of the IDR sequence, but their PhyloP conservation scores are significantly higher compared with surrounding IDR sequences (Figures 6F and 6G), suggesting functional relevance. mRNAs with HC 3′ UTRs are strongly enriched for proteins with HPC-containing IDRs (Figure 6H).

The molecular features of the accompanying IDR basic patches are less clear. IDRs contain more basic patches than FDs, and HPC-containing IDRs contain the most (Figures S7C and S7D). It is unknown whether IDR basic patches require a minimum net charge or distance to HPCs to promote RNA-dependent chaperone activity.

3′ UTRs change protein states of HPC IDR-containing proteins

Our observations suggest that proteins without HPC IDRs fold independently of mRNA 3′ UTRs, whereas 3′ UTRs may affect co-translational folding of HPC IDR-containing proteins. To test this prediction, we transfected CDS vectors with or without FL 3′ UTRs and performed in-cell crosslinking with disuccinimidyl glutarate (DSG), followed by western blot analysis (Figure 7A).

We tested four low-valency mRNAs that encode proteins without IDRs (ENO1, DHPS, RACK1, and EIF3I) and three low-valency mRNAs that encode proteins whose IDRs lack HPCs (SSBP4, SSRP1, and SF3B4; Table S5). We used line profiles and Pearson's correlation coefficients to quantify 3′ UTR-dependent differences in protein crosslinking pattern (Figure 7B). In the tested cases, the crosslinking patterns were nearly identical when the proteins were expressed from mRNA templates with or without 3′ UTRs (Figures 7B, 7D, 7E, S7E, and S7F). The protein crosslinking pattern captures potential differences in protein folding, oligomerization states, or protein interaction partners, suggesting 3′ UTR-independent protein folding of the tested candidates.

In contrast, for all tested HPC IDR-containing proteins encoded by mRNAs with multivalent HC 3′ UTRs, including MYC, UTX, and FOXP2, we observed 3′ UTR-dependent differences in protein crosslinking patterns with Pearson's correlation coefficients $\leq$0.6 (Figures 7C–7E and S7G; Table S5). Inclusion of 3′ UTRs in mRNA templates changes their steady-state protein crosslinking patterns, consistent with co-translational 3′ UTR effects that alter the adopted protein states permanently (Figure 7F).

DISCUSSION

According to Anfinsen's dogma, the amino acid sequence is sufficient for protein folding.[61] This dogma is based on the folding of small, fully structured, single-domain proteins, such as RNase A, which are outliers within the human proteome, as they are smaller than 94% of human proteins (Table S1). Our data contradict this dogma by showing that—in human cells—synthesis of biologically active proteins that contain long IDRs requires both the CDS and 3′ UTR in the mRNA template.

IDRs with hydrophobic clusters potentially misfold during translation

It is currently thought that IDRs do not adopt a single stable conformation in isolation but sample a wide array of distinct conformational states.[27] Our observations indicate that this view may only be partially true for 40% of IDRs (N = 5,300) that contain short regions with clustered hydrophobic amino acids (Figure 6E). Based on in-cell crosslinking data, we propose that HPCs in IDRs potentially cause co-translational protein misfolding, which is prevented by IDR chaperone activity of mesh-like condensate-enriched 3′ UTRs during translation (Figures 4E and 7F). Notably, the intervening IDR segments between the HPCs do not participate in folding and act as classical IDRs (Figures 7F and S3B).

Traditional chaperones prevent misfolding of structured proteins

Chaperones promote the formation of biologically active conformations and minimize off-pathway reactions. Traditionally,

(C) As in (B), but shown is HA-FOXP2.
(D) 3′ UTR-dependent protein crosslinking patterns, shown by line profiles. Raw data in Figures S7E–S7G.
(E) Summary of Pearson's correlation coefficients from (B)–(D).
(F) Model for 3′ UTR-chaperoned control of protein activity. In the absence of 3′ UTR-dependent chaperone activity, proteins with HPC IDRs potentially misfold.

chaperones have been regarded as proteins that prevent misfolding of other proteins, which are usually fully structured single-domain proteins.[62–65] More recently, it was suggested that RNA has protein chaperone activity, as it reduces protein misfolding and aggregation of structured proteins *in vitro*.[66–70] In these cases, RNA prevents aggregation of fully folded proteins without RBRs. As this type of chaperone activity is recapitulated with DNA or polyanions, it is similar to the solubilizing effects of polyD/E proteins,[71] but distinct from the IDR chaperone activity described here.

3′ UTRs act as IDR chaperones and prevent misfolding of IDR-containing proteins

In cellular JMJD3, 77% of IDR crosslinks localize to hydrophobic clusters (Figure 6B). These IDR regions bind to the FD when JMJD3 is generated from a 3′ UTR-lacking mRNA but bind to one another when the 3′ UTR is present (Figures 2H and 2I). The 3′ UTR mimics the function of ATP-independent chaperones, such as trigger factor, which acts as a holdase in bacteria and allows folding within domains and reduces inter-domain misfolding.[23] The differences are that the trigger factor is a protein that acts on FDs, whereas 3′ UTRs are RNA acting on IDRs. Multivalent RNAs in mesh-like condensates have IDR holdase activity, as co-translational RNA–IDR interactions prevent potential interference of hydrophobic IDR clusters with the folding of structured domains. As 3′ UTRs determine the cellular activity of transcriptional regulators in the nucleus, in the most likely scenario, proteins whose IDRs contain hydrophobic clusters adopt irreversible conformations during co-translational folding.

In addition to the 3′ UTR-mediated co-translational IDR chaperone activity described in our study, a similar chaperone activity mediated by RNA was recently reported.[72,73] Therapeutic delivery of short RNAs derived from human 3′ UTRs prevented and dissolved aggregates of the RNA-binding proteins FUS or TDP-43 in cells. In our and their cases, RNA-mediated chaperone activity targets proteins that bind RNA, contain hydrophobic clusters, and have long IDRs. RNA binding prevents detrimental interaction between FDs and IDR hydrophobic clusters, thus preventing aggregation or misfolding.[67,72,73]

Mesh-like condensates are compartments with IDR chaperone activity

Not all 3′ UTRs have IDR chaperone activity (Figure 5B). 3′ UTRs with IDR chaperone activity are multivalent, an RNA feature that allows their enrichment in mesh-like cytoplasmic condensates (Figures 5F and 5H).[12] As 3′ UTRs incapable of localizing mRNAs to mesh-like condensates lack IDR chaperone activity (Figure 5G), mesh-like condensates emerge as cytoplasmic compartments that provide favorable folding environments for IDR-containing proteins. Multivalent 3′ UTRs and condensate-enriched RNA-binding proteins cooperate to generate functional folding compartments (Figure 5K).

Implications for ectopic gene expression studies

3′ UTRs in mRNAs encoding proteins with IDR hydrophobic clusters are extensively conserved (Figures 1A–1D), whereas the 3′ UTRs of mRNAs encoding small, fully folded proteins usually are not conserved. Our work has important implications for cellular studies based on vector constructs. Although genome editing methods exist, ectopic cDNA expression is still widely used for production of recombinant proteins or for studying protein function either in cells or in transgenic animals. As vector technology was developed in the 1970s,[74] when 3′ UTR boundaries were unknown, in nearly all cases, CDS-only vectors were used. Lack of 3′ UTRs has no influence on the folding of fully structured proteins but directs mRNA translation of IDR-containing proteins to the wrong cytoplasmic compartments. HC 3′ UTRs have evolved to target misfolding-prone IDRs to folding environments with RNA-based IDR chaperone activity.

Limitations of the study

Although *in vitro*, RNA–IDR interaction is necessary and sufficient for a change in JMJD3 domain interaction preference, we did not directly show that the *KDM6B* 3′ UTR binds to the JMJD3 nascent chain while being translated in mesh-like condensates.

Although we did not observe differences in codon usage in our JMJD3 deletion constructs (Table S5), we have not directly ruled out that the *KDM6B* 3′ UTR could also influence translation rate with subsequent consequences on protein folding.

Chaperones are molecules that transiently interact with their substrate proteins but are not part of the final product, but this point has not been directly shown by us. However, as multivalent 3′ UTRs are integral components of mesh-like condensates, it is unlikely that they are part of the final protein.

RESOURCE AVAILABILITY

Lead contact

Further information and requests for resources and reagents should be directed to and will be fulfilled by the lead contact, Christine Mayr (mayrc@mskcc.org).

Materials availability

Plasmids generated in this study will be deposited to Addgene. The gene-edited cell lines HeLa *TIAL1* iKO, iPSC 731.2B-Cas9 KDM6B Udel clones, and the corresponding ctrl clones generated in this study are available from the lead contact with a completed materials transfer agreement.

Data and code availability

Computed RNA and protein parameters are reported in Table S1. The processed RNA-seq data for MYC and UTX/KDM6A are reported in Table S2, and their raw data are accessible through GEO: GSE301135. The JMJD3/KDM6B HA and H3K27me3 ChIP-seq data are accessible through GEO: GSE301136. The data of the SILAC co-IP MS and XL-MS experiment have been deposited in the PRIDE repository: PXD074293, PXD072448. The processed data are reported in Table S3. The correlation analysis to identify a surrogate marker for RNA valency is reported in Table S4. The protein and RNA features of the experimentally validated proteins are reported in Table S5. The codon usage ratio of the KDM6B constructs is reported in Table S5. Analysis code for 3′ UTR phyloP conservation, 3′ UTR features, and IDR characteristics were deposited at Zenodo (doi.org/10.5281/zenodo.19226332). Original western blot images, presented microscopy images, and scripts for analysis have been deposited at Mendeley Data (10.17632/6dzvsrbbym.1). FXR1 and TIS11B iCLIP, as well as RNA-seq data from subcytoplasmic fractionation, were downloaded from ArrayExpress: E-MTAB-13545 and GEO: GSE215770, respectively. Any additional information required to reanalyze the data reported in this paper is available from the lead contact upon request.

ACKNOWLEDGMENTS

This work was funded by grants from the Pershing Square Foundation (William Ackman and Neri Oxman), the Mathers Foundation, the NIH Director's Pioneer Award (DP1GM123454), and an NIGMS R35 Award (R35GM144046) to C.M., as well as the MSK Core Grant (P30CA008748). We thank Ting Cai for providing the *KDM6B* 3′ UTR deletion iPSCs and Ellen Horste for the HeLa *TIAL1* iKO and for helping with RNA-FISH. We thank Mervin Fansler for early work on 3′ UTR conservation and help with RNA-seq analysis, Chiara Evans for help with disome extraction, and Jiaxiang Ren for image analysis code. We thank Mara Monetti and Zhuoning Li (Proteomics Core, MSKCC) for MS analysis and useful discussions. We thank Pierre-Jacques Hamard and Richard Koche (ERIL, MSKCC) for the ChIP-seq experiments. We thank all members of the Mayr lab, T.R. Cech (University of Colorado Boulder), N.M. Bonini (University of Pennsylvania), and E. Levy (University of Geneva) for critical reading of the manuscript and helpful discussions.

AUTHOR CONTRIBUTIONS

Y.L. performed all cellular experiments with constructs. Y.Z. performed all *in vitro* assays. M.-C.W. examined the endogenous *KDM6B* 3′ UTR. S.B. performed computational analyses with input from C.M. Y.L. and C.M. conceived the project, designed the experiments, and wrote the manuscript with input from all authors.

DECLARATION OF INTERESTS

Christine Mayr is a member of the *Cell* advisory board.

STAR★METHODS

Detailed methods are provided in the online version of this paper and include the following:

- KEY RESOURCES TABLE
- EXPERIMENTAL MODEL AND STUDY PARTICIPANT DETAILS
  - Cell lines
- METHOD DETAILS
  - Vector constructs
  - Plasmid transfection and viral transduction
  - Western blotting
  - Chemical Crosslinking
  - Crosslinking mass spectrometry
  - SILAC-based co-IP-MS
  - Immunofluorescence staining
  - Lactate accumulation measurement
  - Detect RNA-protein interactions in cells
  - Digitonin RNA-FISH
  - Disome assay
  - iPSC to mesendoderm differentiation
  - Flow cytometry
  - RNA-seq
  - ChIP-seq
  - qRT-PCR
  - Protein purification
  - RNA *in vitro* transcription
  - Fluorescence polarization assay
  - In vitro thiol-thiol crosslinking
  - mRNA feature analysis
  - Protein feature analysis
  - Gene ontology analysis
  - Protein structure prediction
  - RNA-seq analysis
  - ChIP-seq analysis
  - Immunofluorescence staining analysis
  - Digitonin RNA-FISH analysis
  - Amplicon seq analysis
- QUANTIFICATION AND STATISTICAL ANALYSIS

SUPPLEMENTAL INFORMATION

Supplemental information can be found online at https://doi.org/10.1016/j.cell.2026.05.017.

Received: July 3, 2025
Revised: December 31, 2025
Accepted: May 14, 2026
Published: June 8, 2026

REFERENCES

1. Lianoglou, S., Garg, V., Yang, J.L., Leslie, C.S., and Mayr, C. (2013). Ubiquitously transcribed genes use alternative polyadenylation to achieve tissue-specific expression. Genes Dev. *27*, 2380–2396. https://doi.org/10.1101/gad.229328.113.
2. Fansler, M.M., Mitschka, S., and Mayr, C. (2024). Quantifying 3′UTR length from scRNA-seq data reveals changes independent of gene expression. Nat. Commun. *15*, 4050. https://doi.org/10.1038/s41467-024-48254-9.
3. Siepel, A., Bejerano, G., Pedersen, J.S., Hinrichs, A.S., Hou, M., Rosenbloom, K., Clawson, H., Spieth, J., Hillier, L.W., Richards, S., et al. (2005). Evolutionarily conserved elements in vertebrate, insect, worm, and yeast genomes. Genome Res. *15*, 1034–1050. https://doi.org/10.1101/gr.3715005.
4. Litterman, A.J., Kageyama, R., Le Tonqueze, O., Zhao, W., Gagnon, J.D., Goodarzi, H., Erle, D.J., and Ansel, K.M. (2019). A massively parallel 3′ UTR reporter assay reveals relationships between nucleotide content, sequence conservation, and mRNA destabilization. Genome Res. *29*, 896–906. https://doi.org/10.1101/gr.242552.118.
5. Mayr, C., and Bartel, D.P. (2009). Widespread shortening of 3′UTRs by alternative cleavage and polyadenylation activates oncogenes in cancer cells. Cell *138*, 673–684. https://doi.org/10.1016/j.cell.2009.06.016.
6. Berkovits, B.D., and Mayr, C. (2015). Alternative 3′ UTRs act as scaffolds to regulate membrane protein localization. Nature *522*, 363–367. https://doi.org/10.1038/nature14321.
7. Lee, S.H., and Mayr, C. (2019). Gain of Additional BIRC3 Protein Functions through 3′-UTR-Mediated Protein Complex Formation. Mol. Cell *74*, 701–712.e9. https://doi.org/10.1016/j.molcel.2019.03.006.
8. Gasparski, A.N., Moissoglu, K., Pallikkuth, S., Meydan, S., Guydosh, N.R., and Mili, S. (2023). mRNA location and translation rate determine protein targeting to dual destinations. Mol. Cell *83*, 2726–2738.e9. https://doi.org/10.1016/j.molcel.2023.06.036.
9. Chen, C.Y.A., and Shyu, A.B. (1995). AU-rich elements: characterization and importance in mRNA degradation. Trends Biochem. Sci. *20*, 465–470. https://doi.org/10.1016/S0968-0004(00)89102-1.
10. Mitschka, S., and Mayr, C. (2022). Context-specific regulation and function of mRNA alternative polyadenylation. Nat. Rev. Mol. Cell Biol. *23*, 779–796. https://doi.org/10.1038/s41580-022-00507-5.
11. Ma, W., and Mayr, C. (2018). A Membraneless Organelle Associated with the Endoplasmic Reticulum Enables 3′UTR-Mediated Protein-Protein Interactions. Cell *175*, 1492–1506.e19. https://doi.org/10.1016/j.cell.2018.10.007.
12. Ma, W., Zhen, G., Xie, W., and Mayr, C. (2021). In vivo reconstitution finds multivalent RNA-RNA interactions as drivers of mesh-like condensates. eLife *10*, e64252. https://doi.org/10.7554/eLife.64252.
13. Horste, E.L., Fansler, M.M., Cai, T., Chen, X., Mitschka, S., Zhen, G., Lee, F.C.Y., Ule, J., and Mayr, C. (2023). Subcytoplasmic location of translation controls protein output. Mol. Cell *83*, 4509–4523.e11. https://doi.org/10.1016/j.molcel.2023.11.025.
14. Chen, X., Fansler, M.M., Janjoš, U., Ule, J., and Mayr, C. (2024). The FXR1 network acts as a signaling scaffold for actomyosin remodeling. Cell *187*, 5048–5063.e25. https://doi.org/10.1016/j.cell.2024.07.015.

15. Reid, D.W., and Nicchitta, C.V. (2012). Primary role for endoplasmic reticulum-bound ribosomes in cellular translation identified by ribosome profiling. J. Biol. Chem. *287*, 5518–5527. https://doi.org/10.1074/jbc.M111.312280.

16. Fazal, F.M., Han, S., Parker, K.R., Kaewsapsak, P., Xu, J., Boettiger, A.N., Chang, H.Y., and Ting, A.Y. (2019). Atlas of Subcellular RNA Localization Revealed by APEX-Seq. Cell *178*, 473–490.e26. https://doi.org/10.1016/j.cell.2019.05.027.

17. Xia, C., Fan, J., Emanuel, G., Hao, J., and Zhuang, X. (2019). Spatial transcriptome profiling by MERFISH reveals subcellular RNA compartmentalization and cell cycle-dependent gene expression. Proc. Natl. Acad. Sci. USA *116*, 19490–19499. https://doi.org/10.1073/pnas.1912459116.

18. Villanueva, E., Smith, T., Pizzinga, M., Elzek, M., Queiroz, R.M.L., Harvey, R.F., Breckels, L.M., Crook, O.M., Monti, M., Dezi, V., et al. (2024). System-wide analysis of RNA and protein subcellular localization dynamics. Nat. Methods *21*, 60–71. https://doi.org/10.1038/s41592-023-02101-9.

19. Keber, F.C., Nguyen, T., Mariossi, A., Brangwynne, C.P., and Wühr, M. (2024). Evidence for widespread cytoplasmic structuring into mesoscale condensates. Nat. Cell Biol. *26*, 346–352. https://doi.org/10.1038/s41556-024-01363-5.

20. Boraas, L.C., Hu, M., Martino, P., Thornton, L., Vejnar, C.E., Zhen, G., Zeng, L., Parker, D.M., Cox, A.L., Giraldez, A.J., et al. (2025). G3BP1 ribonucleoprotein complexes regulate focal adhesion protein mobility and cell migration. Cell Rep. *44*, 115237. https://doi.org/10.1016/j.celrep.2025.115237.

21. Gasparski, A.N., Mason, D.E., Moissoglu, K., and Mili, S. (2022). Regulation and outcomes of localized RNA translation. WIREs RNA *13*, e1721. https://doi.org/10.1002/wrna.1721.

22. Han, J.-H., Batey, S., Nickson, A.A., Teichmann, S.A., and Clarke, J. (2007). The folding and evolution of multidomain proteins. Nat. Rev. Mol. Cell Biol. *8*, 319–330. https://doi.org/10.1038/nrm2144.

23. Liu, K., Maciuba, K., and Kaiser, C.M. (2019). The Ribosome Cooperates with a Chaperone to Guide Multi-domain Protein Folding. Mol. Cell *74*, 310–319.e7. https://doi.org/10.1016/j.molcel.2019.01.043.

24. Waudby, C.A., Dobson, C.M., and Christodoulou, J. (2019). Nature and Regulation of Protein Folding on the Ribosome. Trends Biochem. Sci. *44*, 914–926. https://doi.org/10.1016/j.tibs.2019.06.008.

25. van der Lee, R., Buljan, M., Lang, B., Weatheritt, R.J., Daughdrill, G.W., Dunker, A.K., Fuxreiter, M., Gough, J., Gsponer, J., Jones, D.T., et al. (2014). Classification of intrinsically disordered regions and proteins. Chem. Rev. *114*, 6589–6631. https://doi.org/10.1021/cr400525m.

26. Davey, N.E. (2019). The functional importance of structure in unstructured protein regions. Curr. Opin. Struct. Biol. *56*, 155–163. https://doi.org/10.1016/j.sbi.2019.03.009.

27. Holehouse, A.S., and Kragelund, B.B. (2024). The molecular basis for cellular function of intrinsically disordered protein regions. Nat. Rev. Mol. Cell Biol. *25*, 187–211. https://doi.org/10.1038/s41580-023-00673-0.

28. Cermakova, K., and Hodges, H.C. (2023). Interaction modules that impart specificity to disordered protein. Trends Biochem. Sci. *48*, 477–490. https://doi.org/10.1016/j.tibs.2023.01.004.

29. Pollard, K.S., Hubisz, M.J., Rosenbloom, K.R., and Siepel, A. (2010). Detection of nonneutral substitution rates on mammalian phylogenies. Genome Res. *20*, 110–121. https://doi.org/10.1101/gr.097857.109.

30. Mészáros, B., Erdős, G., and Dosztányi, Z. (2018). IUPred2A: context-dependent prediction of protein disorder as a function of redox state and protein binding. Nucleic Acids Res. *46*, W329–W337. https://doi.org/10.1093/nar/gky384.

31. Jumper, J., Evans, R., Pritzel, A., Green, T., Figurnov, M., Ronneberger, O., Tunyasuvunakool, K., Bates, R., Žídek, A., Potapenko, A., et al. (2021). Highly accurate protein structure prediction with AlphaFold. Nature *596*, 583–589. https://doi.org/10.1038/s41586-021-03819-2.

32. Sherman, B.T., Hao, M., Qiu, J., Jiao, X., Baseler, M.W., Lane, H.C., Imamichi, T., and Chang, W. (2022). DAVID: a web server for functional enrichment analysis and functional annotation of gene lists (2021 update). Nucleic Acids Res. *50*, W216–W221. https://doi.org/10.1093/nar/gkac194.

33. Minezaki, Y., Homma, K., Kinjo, A.R., and Nishikawa, K. (2006). Human transcription factors contain a high fraction of intrinsically disordered regions essential for transcriptional regulation. J. Mol. Biol. *359*, 1137–1149. https://doi.org/10.1016/j.jmb.2006.04.016.

34. Dhar, S.S., Lee, S.H., Chen, K., Zhu, G., Oh, W., Allton, K., Gafni, O., Kim, Y.Z., Tomoiga, A.S., Barton, M.C., et al. (2016). An essential role for UTX in resolution and activation of bivalent promoters. Nucleic Acids Res. *44*, 3659–3674. https://doi.org/10.1093/nar/gkv1516.

35. Revia, S., Seretny, A., Wendler, L., Banito, A., Eckert, C., Breuer, K., Mayakonda, A., Lutsik, P., Evert, M., Ribback, S., et al. (2022). Histone H3K27 demethylase KDM6A is an epigenetic gatekeeper of mTORC1 signalling in cancer. Gut *71*, 1613–1628. https://doi.org/10.1136/gutjnl-2021-325405.

36. Huppertz, I., Perez-Perri, J.I., Mantas, P., Sekaran, T., Schwarzl, T., Russo, F., Ferring-Appel, D., Koskova, Z., Dimitrova-Paternoga, L., Kafkia, E., et al. (2022). Riboregulation of Enolase 1 activity controls glycolysis and embryonic stem cell differentiation. Mol. Cell *82*, 2666–2680.e11. https://doi.org/10.1016/j.molcel.2022.05.019.

37. Zhou, J., Pang, J., Tripathi, M., Ho, J.P., Widjaja, A.A., Shekeran, S.G., Cook, S.A., Suzuki, A., Diehl, A.M., Petretto, E., et al. (2022). Spermidine-mediated hypusination of translation factor EIF5A improves mitochondrial fatty acid oxidation and prevents non-alcoholic steatohepatitis progression. Nat. Commun. *13*, 5202. https://doi.org/10.1038/s41467-022-32788-x.

38. Agger, K., Cloos, P.A.C., Christensen, J., Pasini, D., Rose, S., Rappsilber, J., Issaeva, I., Canaani, E., Salcini, A.E., and Helin, K. (2007). UTX and JMJD3 are histone H3K27 demethylases involved in HOX gene regulation and development. Nature *449*, 731–734. https://doi.org/10.1038/nature06145.

39. Xiang, Y., Zhu, Z., Han, G., Lin, H., Xu, L., and Chen, C.D. (2007). JMJD3 is a histone H3K27 demethylase. Cell Res. *17*, 850–857. https://doi.org/10.1038/cr.2007.83.

40. Ohtani, K., Zhao, C., Dobreva, G., Manavski, Y., Kluge, B., Braun, T., Rieger, M.A., Zeiher, A.M., and Dimmeler, S. (2013). Jmjd3 controls mesodermal and cardiovascular differentiation of embryonic stem cells. Circ. Res. *113*, 856–862. https://doi.org/10.1161/circresaha.113.302035.

41. Bisson, J.A., Gordillo, M., Kumar, R., de Silva, N., Yang, E., Banks, K.M., Shi, Z.D., Lee, K., Yang, D., Chung, W.K., et al. (2025). GATA6 regulates WNT and BMP programs to pattern precardiac mesoderm during the earliest stages of human cardiogenesis. eLife *13*. https://doi.org/10.7554/eLife.100797.

42. Kruidenier, L., Chung, C.W., Cheng, Z., Liddle, J., Che, K., Joberty, G., Bantscheff, M., Bountra, C., Bridges, A., Diallo, H., et al. (2012). A selective jumonji H3K27 demethylase inhibitor modulates the proinflammatory macrophage response. Nature *488*, 404–408. https://doi.org/10.1038/nature11262.

43. De Santa, F., Totaro, M.G., Prosperini, E., Notarbartolo, S., Testa, G., and Natoli, G. (2007). The histone H3 lysine-27 demethylase Jmjd3 links inflammation to inhibition of polycomb-mediated gene silencing. Cell *130*, 1083–1094. https://doi.org/10.1016/j.cell.2007.08.019.

44. Miller, S.A., Mohn, S.E., and Weinmann, A.S. (2010). Jmjd3 and UTX play a demethylase-independent role in chromatin remodeling to regulate T-box family member-dependent gene expression. Mol. Cell *40*, 594–605. https://doi.org/10.1016/j.molcel.2010.10.028.

45. Yang, M., Wang, C., Zhou, M., Bao, L., Wang, Y., Kumar, A., Xing, C., Luo, W., and Wang, Y. (2022). KDM6B promotes PARthanatos via suppression of O6-methylguanine DNA methyltransferase repair and sustained checkpoint response. Nucleic Acids Res. *50*, 6313–6331. https://doi.org/10.1093/nar/gkac471.

46. Nussinov, R., Liu, Y., Zhang, W., and Jang, H. (2023). Protein conformational ensembles in function: roles and mechanisms. RSC Chem. Biol. *4*, 850–864. https://doi.org/10.1039/d3cb00114h.

47. Castello, A., Fischer, B., Frese, C.K., Horos, R., Alleaume, A.M., Foehr, S., Curk, T., Krijgsveld, J., and Hentze, M.W. (2016). Comprehensive Identification of RNA-Binding Domains in Human Cells. Mol. Cell *63*, 696–710. https://doi.org/10.1016/j.molcel.2016.06.029.

48. Oksuz, O., Henninger, J.E., Warneford-Thomson, R., Zheng, M.M., Erb, H., Vancura, A., Overholt, K.J., Hawken, S.W., Banani, S.F., Lauman, R., et al. (2023). Transcription factors interact with RNA to regulate genes. Mol. Cell *83*, 2449–2463.e13. https://doi.org/10.1016/j.molcel.2023.06.012.

49. Zarnegar, B.J., Flynn, R.A., Shen, Y., Do, B.T., Chang, H.Y., and Khavari, P.A. (2016). irCLIP platform for efficient characterization of protein–RNA interactions. Nat. Methods *13*, 489–492. https://doi.org/10.1038/nmeth.3840.

50. Gokhale, N.S., Sam, R.K., Somfleth, K., Thompson, M.G., Marciniak, D.M., Smith, J.R., Genoyer, E., Eggenberger, J., Chu, L.H., Park, M., et al. (2024). Cellular RNA interacts with MAVS to promote antiviral signaling. Science *386*, eadl0429. https://doi.org/10.1126/science.adl0429.

51. Remaut, H., and Waksman, G. (2006). Protein-protein interaction through beta-strand addition. Trends Biochem. Sci. *31*, 436–444. https://doi.org/10.1016/j.tibs.2006.06.007.

52. Abramson, J., Adler, J., Dunger, J., Evans, R., Green, T., Pritzel, A., Ronneberger, O., Willmore, L., Ballard, A.J., Bambrick, J., et al. (2024). Accurate structure prediction of biomolecular interactions with AlphaFold 3. Nature *630*, 493–500. https://doi.org/10.1038/s41586-024-07487-w.

53. Mena, E.L., Jevtić, P., Greber, B.J., Gee, C.L., Lew, B.G., Akopian, D., Nogales, E., Kuriyan, J., and Rape, M. (2020). Structural basis for dimerization quality control. Nature *586*, 452–456. https://doi.org/10.1038/s41586-020-2636-7.

54. Bertolini, M., Fenzl, K., Kats, I., Wruck, F., Tippmann, F., Schmitt, J., Auburger, J.J., Tans, S., Bukau, B., and Kramer, G. (2021). Interactions between nascent proteins translated by adjacent ribosomes drive homomer assembly. Science *371*, 57–64. https://doi.org/10.1126/science.abc7151.

55. Mallik, S., Venezian, J., Lobov, A., Heidenreich, M., Garcia-Seisdedos, H., Yeates, T.O., Shiber, A., and Levy, E.D. (2025). Structural determinants of co-translational protein complex assembly. Cell *188*, 764–777.e22. https://doi.org/10.1016/j.cell.2024.11.013.

56. Wu, C.C.-C., Peterson, A., Zinshteyn, B., Regot, S., and Green, R. (2020). Ribosome Collisions Trigger General Stress Responses to Regulate Cell Fate. Cell *182*, 404–416.e14. https://doi.org/10.1016/j.cell.2020.06.006.

57. Zhao, T., Chen, Y.M., Li, Y., Wang, J., Chen, S., Gao, N., and Qian, W. (2021). Disome-seq reveals widespread ribosome collisions that promote cotranslational protein folding. Genome Biol. *22*, 16. https://doi.org/10.1186/s13059-020-02256-0.

58. Poudyal, R.R., Sieg, J.P., Portz, B., Keating, C.D., and Bevilacqua, P.C. (2021). RNA sequence and structure control assembly and function of RNA condensates. Rna *27*, 1589–1601. https://doi.org/10.1261/rna.078875.121.

59. Seim, I., Zhang, V., Jalihal, A.P., Stormo, B.M., Cole, S.J., Ekena, J., Nguyen, H.T., Thirumalai, D., and Gladfelter, A.S. (2024). RNA encodes physical information. Preprint at bioRxiv. https://doi.org/10.1101/2024.12.11.627970.

60. Wang, Z., Kayikci, M., Briese, M., Zarnack, K., Luscombe, N.M., Rot, G., Zupan, B., Curk, T., and Ule, J. (2010). iCLIP predicts the dual splicing effects of TIA-RNA interactions. PLOS Biol. *8*, e1000530. https://doi.org/10.1371/journal.pbio.1000530.

61. Anfinsen, C.B. (1973). Principles that govern the folding of protein chains. Science *181*, 223–230. https://doi.org/10.1126/science.181.4096.223.

62. Dobson, C.M. (2003). Protein folding and misfolding. Nature *426*, 884–890. https://doi.org/10.1038/nature02261.

63. Quan, S., and Bardwell, J.C.A. (2012). Chaperone discovery. BioEssays *34*, 973–981. https://doi.org/10.1002/bies.201200059.

64. Horwich, A.L. (2014). Molecular Chaperones in Cellular Protein Folding: The Birth of a Field. Cell *157*, 285–288. https://doi.org/10.1016/j.cell.2014.03.029.

65. Balchin, D., Hayer-Hartl, M., and Hartl, F.U. (2020). Recent advances in understanding catalysis of protein folding by molecular chaperones. FEBS Lett. *594*, 2770–2781. https://doi.org/10.1002/1873-3468.13844.

66. Choi, S.I., Han, K.S., Kim, C.W., Ryu, K.S., Kim, B.H., Kim, K.H., Kim, S.I., Kang, T.H., Shin, H.C., Lim, K.H., et al. (2008). Protein solubility and folding enhancement by interaction with RNA. PLOS One *3*, e2677. https://doi.org/10.1371/journal.pone.0002677.

67. Sun, Y., Arslan, P.E., Won, A., Yip, C.M., and Chakrabartty, A. (2014). Binding of TDP-43 to the 3′UTR of Its Cognate mRNA Enhances Its Solubility. Biochemistry *53*, 5885–5894. https://doi.org/10.1021/bi500617x.

68. Gray, M.J., Wholey, W.-Y., Wagner, N.O., Cremers, C.M., Mueller-Schickert, A., Hock, N.T., Krieger, A.G., Smith, E.M., Bender, R.A., Bardwell, J.C.A., et al. (2014). Polyphosphate Is a Primordial Chaperone. Mol. Cell *53*, 689–699. https://doi.org/10.1016/j.molcel.2014.01.012.

69. Docter, B.E., Horowitz, S., Gray, M.J., Jakob, U., and Bardwell, J.C.A. (2016). Do nucleic acids moonlight as molecular chaperones? Nucleic Acids Res. *44*, 4835–4845. https://doi.org/10.1093/nar/gkw291.

70. Litberg, T.J., and Horowitz, S. (2024). Roles of Nucleic Acids in Protein Folding, Aggregation, and Disease. ACS Chem. Biol. *19*, 809–823. https://doi.org/10.1021/acschembio.3c00695.

71. Huang, L., Agrawal, T., Zhu, G., Yu, S., Tao, L., Lin, J., Marmorstein, R., Shorter, J., and Yang, X. (2021). DAXX represents a new type of protein-folding enabler. Nature *597*, 132–137. https://doi.org/10.1038/s41586-021-03824-5.

72. Guo, L., Mann, J.R., Mauna, J.C., Copley, K.E., Wang, H., Rubien, J.D., Bergmann, C.A., Carey, J.L., Merjane, J., Ngo, M., et al. (2026). Defining RNA oligonucleotides that reverse deleterious phase transitions of RNA-binding proteins with prion-like domains. Mol. Cell *86*, 114–134.e10. https://doi.org/10.1016/j.molcel.2025.12.009.

73. Copley, K.E., Mauna, J.C., Danielson, H.L., Chen, Q., Ozguney, B., Ngo, M., Xie, L., Smirnov, A., Davis, M., Mayne, L., et al. (2026). Short RNA chaperones promote aggregation-resistant TDP-43 conformers to mitigate neurodegeneration. Science *392*, eadv3301. https://doi.org/10.1126/science.adv3301.

74. Cohen, S.N., Chang, A.C.Y., Boyer, H.W., and Helling, R.B. (1973). Construction of Biologically Functional Bacterial Plasmids *In Vitro*. Proc. Natl. Acad. Sci. USA *70*, 3240–3244. https://doi.org/10.1073/pnas.70.11.3240.

75. Cai, T., Cruz, N.M., Basu, S., White, R.M., and Mayr, C. (2026). Intermolecular 3′UTR-3′UTR interactions drive Wnt gene activation through heteromeric protein assembly. Preprint at bioRxiv. https://doi.org/10.64898/2026.05.05.723075.

76. Sarbassov, D.D., Guertin, D.A., Ali, S.M., and Sabatini, D.M. (2005). Phosphorylation and regulation of Akt/PKB by the rictor-mTOR complex. Science *307*, 1098–1101. https://doi.org/10.1126/science.1106148.

77. Schindelin, J., Arganda-Carreras, I., Frise, E., Kaynig, V., Longair, M., Pietzsch, T., Preibisch, S., Rueden, C., Saalfeld, S., Schmid, B., et al. (2012). Fiji: an open-source platform for biological-image analysis. Nat. Methods *9*, 676–682. https://doi.org/10.1038/nmeth.2019.

78. Holehouse, A.S., Das, R.K., Ahad, J.N., Richardson, M.O.G., and Pappu, R.V. (2017). CIDER: Resources to Analyze Sequence-Ensemble Relationships of Intrinsically Disordered Proteins. Biophys. J. *112*, 16–21. https://doi.org/10.1016/j.bpj.2016.11.3200.

79. van der Walt, S., Schönberger, J.L., Nunez-Iglesias, J., Boulogne, F., Warner, J.D., Yager, N., Gouillart, E., and Yu, T. (2014). scikit-image: image processing in Python. PeerJ *2*, e453. https://doi.org/10.7717/peerj.453.

80. Goddard, T.D., Huang, C.C., Meng, E.C., Pettersen, E.F., Couch, G.S., Morris, J.H., and Ferrin, T.E. (2018). UCSF ChimeraX: Meeting modern challenges in visualization and analysis. Protein Sci. *27*, 14–25. https://doi.org/10.1002/pro.3235.

81. Patro, R., Duggal, G., Love, M.I., Irizarry, R.A., and Kingsford, C. (2017). Salmon provides fast and bias-aware quantification of transcript expression. Nat. Methods *14*, 417–419. https://doi.org/10.1038/nmeth.4197.

82. Soneson, C., Love, M.I., and Robinson, M.D. (2015). Differential analyses for RNA-seq: transcript-level estimates improve gene-level inferences. F1000Res *4*, 1521. https://doi.org/10.12688/f1000research.7563.2.

83. Love, M.I., Huber, W., and Anders, S. (2014). Moderated estimation of fold change and dispersion for RNA-seq data with DESeq2. Genome Biol. *15*, 550. https://doi.org/10.1186/s13059-014-0550-8.

84. Kolde, R. (2025) Pheatmap: Pretty Heatmaps. https://doi.org/10.32614/CRAN.package.pheatmap.

85. Krueger, F., James, F., Ewels, P., Afyounian, E., and Schuster-Boeckler, B. (2021). Trim Galore! Consistent adapter and quality trimming for FASTQ files. https://doi.org/10.5281/zenodo.5603393

86. Langmead, B., and Salzberg, S.L. (2012). Fast gapped-read alignment with Bowtie 2. Nat. Methods *9*, 357–359. https://doi.org/10.1038/nmeth.1923.

87. Gaspar, J.M. (2018). Improved peak-calling with MACS2. Preprint at bioRxiv, 496521. https://doi.org/10.1101/496521.

88. Quinlan, A.R., and Hall, I.M. (2010). BEDTools: a flexible suite of utilities for comparing genomic features. Bioinformatics *26*, 841–842. https://doi.org/10.1093/bioinformatics/btq033.

89. Ramírez, F., Ryan, D.P., Grüning, B., Bhardwaj, V., Kilpert, F., Richter, A.S., Heyne, S., Dündar, F., and Manke, T. (2016). deepTools2: a next generation web server for deep-sequencing data analysis. Nucleic Acids Res. *44*, W160–W165. https://doi.org/10.1093/nar/gkw257.

90. Zhang, J., Kobert, K., Flouri, T., and Stamatakis, A. (2013). PEAR: a fast and accurate Illumina Paired-End reAd mergeR. Bioinformatics *30*, 614–620. https://doi.org/10.1093/bioinformatics/btt593.

91. Shen, W., Le, S., Li, Y., and Hu, F. (2016). SeqKit: A Cross-Platform and Ultrafast Toolkit for FASTA/Q File Manipulation. PLOS One *11*, e0163962. https://doi.org/10.1371/journal.pone.0163962.

92. Chen, Z.L., Meng, J.M., Cao, Y., Yin, J.L., Fang, R.Q., Fan, S.B., Liu, C., Zeng, W.F., Ding, Y.H., Tan, D., et al. (2019). A high-speed search engine pLink 2 with systematic evaluation for proteome-scale identification of cross-linked peptides. Nat. Commun. *10*, 3404. https://doi.org/10.1038/s41467-019-11337-z.

93. Cox, J., and Mann, M. (2008). MaxQuant enables high peptide identification rates, individualized p.p.b.-range mass accuracies and proteome-wide protein quantification. Nat. Biotechnol. *26*, 1367–1372. https://doi.org/10.1038/nbt.1511.

94. Afroz, T., Hock, E.M., Ernst, P., Foglieni, C., Jambeau, M., Gilhespy, L.A.B., Laferriere, F., Maniecka, Z., Plückthun, A., Mittl, P., et al. (2017). Functional and dynamic polymerization of the ALS-linked protein TDP-43 antagonizes its pathologic aggregation. Nat. Commun. *8*, 45. https://doi.org/10.1038/s41467-017-00062-0.

95. Combe, C.W., Graham, M., Kolbowski, L., Fischer, L., and Rappsilber, J. (2024). xiVIEW: Visualisation of Crosslinking Mass Spectrometry Data. J. Mol. Biol. *436*, 168656. https://doi.org/10.1016/j.jmb.2024.168656.

96. Lian, X., Zhang, J., Azarin, S.M., Zhu, K., Hazeltine, L.B., Bao, X., Hsiao, C., Kamp, T.J., and Palecek, S.P. (2013). Directed cardiomyocyte differentiation from human pluripotent stem cells by modulating Wnt/β-catenin signaling under fully defined conditions. Nat. Protoc. *8*, 162–175. https://doi.org/10.1038/nprot.2012.150.

97. Morales, J., Pujar, S., Loveland, J.E., Astashyn, A., Bennett, R., Berry, A., Cox, E., Davidson, C., Ermolaeva, O., Farrell, C.M., et al. (2022). A joint NCBI and EMBL-EBI transcript set for clinical genomics and research. Nature *604*, 310–315. https://doi.org/10.1038/s41586-022-04558-8.

98. Heinz, S., Benner, C., Spann, N., Bertolino, E., Lin, Y.C., Laslo, P., Cheng, J.X., Murre, C., Singh, H., and Glass, C.K. (2010). Simple combinations of lineage-determining transcription factors prime cis-regulatory elements required for macrophage and B cell identities. Mol. Cell *38*, 576–589. https://doi.org/10.1016/j.molcel.2010.05.004.

99. Hofacker, I.L. (2003). Vienna RNA secondary structure server. Nucleic Acids Res. *31*, 3429–3431. https://doi.org/10.1093/nar/gkg599.

100. Forrest, M.E., Pinkard, O., Martin, S., Sweet, T.J., Hanson, G., and Coller, J. (2020). Codon and amino acid content are associated with mRNA stability in mammalian cells. PLOS One *15*, e0228730. https://doi.org/10.1371/journal.pone.0228730.

101. Subramanian, K., Payne, B., Feyertag, F., and Alvarez-Ponce, D. (2022). The Codon Statistics Database: A Database of Codon Usage Bias. Mol. Biol. Evol. *39*. https://doi.org/10.1093/molbev/msac157.

102. Manavalan, P., and Ponnuswamy, P.K. (1978). Hydrophobic character of amino acid residues in globular proteins. Nature *275*, 673–674. https://doi.org/10.1038/275673a0.

STAR★METHODS

KEY RESOURCES TABLE

REAGENT or RESOURCE	SOURCE	IDENTIFIER
Antibodies		
Mouse monoclonal anti-GAPDH	Sigma-Aldrich	Cat#G8795, RRID: AB_1078991
Mouse monoclonal anti-α-Tubulin	Sigma-Aldrich	Cat#T9026, RRID: AB_477593
Rabbit polyclonal anti-Actin	Sigma-Aldrich	Cat#A-2066, RRID: AB_476693
Chicken polyclonal anti-GFP	abcam	Cat#ab13970, RRID: AB_300798
Rabbit polyclonal anti-UTX	Bethyl	Cat#A302-374A, RRID: AB_1907257
Mouse monoclonal anti-HA	Covance	Cat#MMS-101P, RRID: AB_2314672
Rabbit monoclonal anti-HA	Cell Signaling Technology	Cat# 3724, RRID: AB_1549585
Rabbit monoclonal anti-H3K27me3	Cell Signaling Technology	Cat# 9733, RRID: AB_2616029
Mouse monoclonal anti-Puromycin	Sigma-Aldrich	Cat# MABE343, RRID: AB_2566826
Rabbit polyclonal anti-RPLP0	Antibodies Online	Cat#ABIN310003
Rabbit polyclonal anti-Hypusine	Sigma-Aldrich	Cat# ABS1064-I
Rabbit monoclonal anti-eIF5A	Cell Signaling Technology	Cat# 20765, RRID:AB_2798849
Rabbit polyclonal anti-ZAK	Thermo Fisher Scientific	Cat# A301-993A, RRID:AB_1576612
Mouse anti-TIAR	BD Biosciences	Cat# 610352, RRID:AB_397742
Mouse monoclonal anti-TIA1	Santa Cruz Biotechnology	Cat# sc-166247, RRID:AB_2201545
Rabbit polyclonal JMJD3 antibody	abcam	Cat# ab169197, RRID:AB_3676091
IRDye 680RD Donkey anti-Chicken	LI-COR	Cat# 926-68075, RRID: AB_10974977
IRDye 680RD Goat anti-Mouse	LI-COR	Cat# 926-68070, RRID: AB_10956588
IRDye 800CW Donkey anti-Rabbit	LI-COR	Cat# 926-32213, RRID: AB_621848
Donkey anti-Mouse, Alexa Fluor 488	Thermo Fisher	Cat# A-21202, RRID: AB_141607
Donkey anti-Rabbit, Alexa Fluor™ 647	Thermo Fisher	Cat# A-31573, RRID:AB_2536183
Goat anti-Rabbit, Alexa Fluor™ 647	Thermo Fisher	Cat# A-21244, RRID: AB_2535812
PE goat polyclonal anti-Brachyury	R&D Systems	Cat# IC2085A, RRID:AB_2891298
BV421 mouse anti-EOMES	BD Biosciences	Cat# 567166, RRID:AB_2916483
FITC rabbit polyclonal anti-JMJD3	Novus	Cat# NBP1-06640F, RRID:AB_3199312
PE rabbit monoclonal anti-GATA6	Cell Signaling Technology	Cat# 26452, RRID:AB_2798924
Bacterial and virus strains		
BL21(DE3) Competent *E.coli*	NEB	Cat# C2527H
Chemicals, peptides, and recombinant proteins		
Stellaris FISH Probes, eGFP with Quasar 670 Dye	Biosearchtech	Cat# VSMF-1015-5
Lipofectamine 3000	Thermo Fisher	Cat# L3000001
FuGENE	Promega	Cat# E2311
Q5 High-Fidelity DNA Polymerase	NEB	Cat# M0491L
NEBuilder HiFi DNA Assembly Master Mix	NEB	Cat# E2621L
TRI Reagent Solution	Invitrogen	Cat# AM9738
Laemmli SDS sample buffer, reducing (6x)	Thermo Fisher	Cat# J61337.AC
NuPAGE 4-12% Bis-Tris Protein Gels, 1.0 mm, 12 well	Invitrogen	Cat# NP0322
NuPAGE 3 to 8%, Tris-Acetate Mini Protein Gels, 1.0 mm, 12 well	Invitrogen	Cat# EA03752
Novex Tris-Glycine Mini Protein Gels, 8%, 1.0 mm, 12 well	Invitrogen	Cat# XP00082

(*Continued on next page*)

Continued

REAGENT or RESOURCE	SOURCE	IDENTIFIER
Novex Tris-Glycine Mini Protein Gels, 6%, 1.0 mm, 12 well	Invitrogen	Cat# XP00062
NuPAGE MES SDS running buffer 20x	Invitrogen	Cat# NP0002
NuPAGE Tris-Acetate SDS running buffer 20x	Invitrogen	Cat# LA0041
NuPAGE Transfer Buffer (20X)	Invitrogen	Cat# NP00061
Novex Tris-Glycine SDS running buffer 10x	Invitrogen	Cat# LC2675
Odyssey blocking buffer (PBS)	LI-COR	Cat# 927-40000
Polybrene (hexadimethrine bromide)	Sigma-Aldrich	Cat# H9268
16% Paraformaldehde Aqueous Solution	Fisher Scientific	Cat# 50-980-487
Digitonin	Sigma-Aldrich	Cat# D141
SUPERase·In™ RNase Inhibitor	Invitrogen	Cat# AM2694
cOmplete EDTA-free Protease Inhibitor Cocktail	Roche	Cat# 04693159001 or Cat# 11836170001
Pierce™ Anti-HA Magnetic Beads	Thermo Fisher	Cat# 88836
LIVE/DEAD™ Fixable Near-IR Dead Cell Stain Kit	Thermo Fisher	Cat# L10119
LIVE/DEAD™ Fixable Near IR (780) Viability Kit	Thermo Fisher	Cat# L34994
Puromycin	Millipore Sigma	Cat# 54-041-1
Cycloheximide	Sigma-Aldrich	Cat# C7698
Glycine	Fisher Scientific	Cat# BP381-1
D-Sucrose	Fisher Scientific	Cat# BP220-1
Ampicillin Sodium Salt	Fisher Scientific	Cat# BP176025
Kanamycin disulfate salt	Sigma-Aldrich	Cat# K1876
Sodium Chloride	Fisher Scientific	Cat# S271-3
Tris base	Fisher Scientific	Cat# BP152-1
Protein G Dynabeads	Thermo Fisher	Cat# 10004D
KMet SNAP-ChIP Panel	Epicypher	Cat# 191100
Triton X-100	Fisher Scientific	Cat# BP151-100
Tween-20	Fisher Scientific	Cat# BP337-500
Na-deoxycholate	Fisher Scientific	Cat# BP349-100
SPRIselect magnetic beads	Beckman Coulter	Cat# B23318
Bovine Serum Albumin (BSA)	Fisher Scientific	Cat# BP1605100
Dextran Sulfate Sodium Salt	Spectrum Chemical	Cat# DE131
Ribonucleoside Vanadyl Complex	NEB	Cat# S1402
Salmon testes single stranded DNA	Sigma-Aldrich	Cat# D9156
Yeast tRNA	Life Technologies	Cat# 15401029
Formamide	Millipore Sigma	Cat# S4117
TURBO DNase	Life Technologies	Cat# AM2238
RNase I	Life Technologies	Cat# AM2295
Trichloroacetic Acid (TCA)	TCI America	Cat# T0369500G
TALON Metal Affinity Resin	Takara	Cat# 635503
LB media	Fisher Scientific	Cat# BP1426-2
IPTG (Isopropyl-β-D-thiogalactopyranoside, dioxane free)	RPI research	Cat# I56000-25.0
PMSF (Benzylsulfonyl Fluoride)	Sigma Aldrich	Cat# 78830
Lysozyme	Thermo Fisher	Cat# 89833
DNase I	Sigma-Aldrich	Cat# 10104159001
Halt protease inhibitor cocktail	Thermo Fisher	Cat# 78439

(*Continued on next page*)

Continued

REAGENT or RESOURCE	SOURCE	IDENTIFIER
Imidazole	Fisher Scientific	Cat# O3196-500
Tris(2-carboxyethyl)phosphine hydrochloride (TCEP)	Sigma-Aldrich	Cat# C4706
Strep-Tactin® 4Flow® high-capacity resin	Iba life sciences	Cat# 2-1250-010
d-Desthiobiotin	Sigma-Aldrich	Cat# D1411
Cy5-UTP	Enzo life sciences	Cat# ENZ-42506
Streptavidin 680	LI-COR	Cat# 926-68079
DSG	Thermo Fisher	Cat# 20593
BS3 (bis(sulfosuccinimidyl)suberate)	Thermo Fisher	Cat# 21580
ProLong Gold Antifade Mountant with DAPI DNA stain	Thermo Fisher	Cat# P36935
BMOE (bismaleimidoethane)	Thermo Fisher	Cat# 22323
Ethanol	Fisher Scientific	Cat# BP28184
DTT (dithiothreitol)	Life Technologies	Cat# R0862
Nonidet P-40	Sigma-Aldrich	Cat# 74385
HEPES	Sigma-Aldrich	Cat# H4034
Magnesium Chloride Hexahydrate	Fisher Scientific	Cat# M33-500
Potassium Chloride	Sigma-Aldrich	Cat# P9541
Glycerol	Sigma-Aldrich	Cat# G5516
DMEM, free of phenol red and FBS	Thermo Fisher	Cat# 21063029
qScript cDNA SuperMix	Quantabio	Cat# 95048
PowerUp SYBR™ Green Master Mix	Thermo Fisher	Cat# A25742
4x LDS Sample buffer	Thermo Fisher	Cat# J61942.AD
IRDye® 800CW DBCO Infrared Dye	LI-COR	Cat# 929-50000
5′ DNA Adenylation Kit	NEB	Cat# 2610
T4 RNA Ligase 1 (ssRNA Ligase)	NEB	Cat# M0204
T4 PNK	NEB	Cat# M0201
RNase A, DNase and protease-free (10 mg/mL)	Thermo Fisher	Cat# EN0531
SureCast™ Acrylamide Solution (40%)	Thermo Fisher	Cat# HC2040
Phos-tag (TM) Acrylamide AAL-107	FUJIFILM Irvine Scientific	Cat# 30093523
PEG 400	Sigma Aldrich	Cat# PX1286B
Manganese(II) chloride	Sigma-Aldrich	Cat# 244589
Phosphatase Inhibitor Cocktail (100X)	Cell Signaling Technology	Cat# 5870
SimplyBlue SafeStain	Invitrogen	Cat# LC6060
Y-27632 (Dihydrochloride)	StemCell Technologies	Cat# 100-1044
RPMI 1640 Medium	Thermo Fisher	Cat# 11875093
B-27 Supplement, minus insulin	Thermo Fisher	Cat# A1895601
B-27 Supplement	Thermo Fisher	Cat# 17504044
CHIR99021	StemCell Technologies	Cat# 100-1042
Doxycycline	Acros Organics	Cat# 446060050
Lipofectamine RNAiMAX	Thermo Fisher	Cat# 13778150
L-Arginine-HCl	Thermo Fisher	Cat# 89989
L-Lysine-2HCl	Thermo Fisher	Cat# 89987
L-Arginine-HCl (13C6, 99%; 15N4, 99%)	Cambridge Isotope Laboratories	Cat# CNLM-539-H-0.05
L-Lysine-2HCl (13C6, 99%)	Thermo Fisher	Cat# 1860969
Fetal Bovine Serum, dialyzed	Gibco	Cat# A3382001
DMEM for SILAC	Thermo Fisher	Cat# 88364
Critical commercial assays		
Pierce™ BCA Protein Assay Kit	Thermo Fisher	Cat# 23227

(*Continued on next page*)

Continued

REAGENT or RESOURCE	SOURCE	IDENTIFIER
ChIP DNA Clean & Concentrator kit	Zymo Research	Cat# D5205
ThruPLEX®DNA-Seq kit	Takara	Cat# R400676
MEGAscript T7 Transcription kit	Invitrogen	Cat# AM1334
Lactate Assay Kit	Sigma-Aldrich	Cat# MAK570
Deposited data		
RNA-seq datasets	This paper	GEO: GSE301135
KDM6B ChIP-seq	This paper	GEO: GSE301136
XL-MS	This paper	PRIDE: PXD072448
SILAC-IP-MS	This paper	PRIDE: PXD074293
Original code for data analysis	This paper	http://doi.org/10.5281/zenodo.19226332
Raw images and analysis scripts	This paper; Mendeley Data	https://doi.org/10.17632/6dzvsrbbym.1
RNA-seq from subcytoplasmic fractionation and TIS11B iCLIP	Horste et al.[13]	GEO: GSE215770
FXR1 iCLIP data	Chen et al.[14]	ArrayExpress: E-MTAB-13545
Experimental models: Cell lines		
HeLa	Jonathan S.Weissman	N/A
MCF7	Robert Weinberg	N/A
U2OS	Thijn Brummelkamp	N/A
HeLa *TIAL1* iKO	This paper	N/A
Human iPSC 731.2B	SKI Stem Cell Research Core	N/A
iPSC KDM6B Udel	This paper; Cai et al.[75]	N/A
Oligonucleotides		
PCR primers, sgRNA, and shRNA oligos	This paper	Table S6
Recombinant DNA		
pcDNA3.1-puro-mycProm-EGFP	This paper	N/A
pcDNA3.1-puro-mycProm-EGFP-MYC-NU	This paper	N/A
pcDNA3.1-puro-mycProm-EGFP-MYC-U	This paper	N/A
pcDNA3.1-puro-EGFP-MYC-NU	This paper	N/A
pcDNA3.1-puro-EGFP-MYC-U	This paper	N/A
pcDNA3.1-puro-mGFP-KDM6A-NU	This paper	N/A
pcDNA3.1-puro-mGFP-KDM6A-U	This paper	N/A
pcDNA3.1-puro-mGFP-KDM6B-NU	This paper	N/A
pcDNA3.1-puro-mGFP-KDM6B-U	This paper	N/A
pcDNA3.1-puro-mGFP-KDM6B-IDH1-UTR	This paper	N/A
pcDNA3.1-puro-mGFP-KDM6B-HSPA1B-UTR	This paper	N/A
pcDNA3.1-puro-mGFP-KDM6B-MAP2K2-UTR	This paper	N/A
pcDNA3.1-puro-mGFP-KDM6B-PIN1-UTR	This paper	N/A
pCMV-HA-KDM6B	Agger et al.[38]	Addgene Plasmid #24167
pCMV-HA-KDM6A	Agger et al.[38]	Addgene Plasmid #24168
pCMV-HA-KDM6B-U	This work	N/A
pCMV-HA-KDM6A-U	This work	N/A
pCMV-HA-KDM6A-shResistant-NU	This work	N/A
pCMV-HA-KDM6A-shResistant-U	This work	N/A
pCMV-HA-KDM6B-IDH1-UTR	This work	N/A
pCMV-HA-KDM6B-HSPA1B-UTR	This work	N/A
pCMV-HA-KDM6B-MAP2K2-UTR	This work	N/A
pCMV-HA-KDM6B-PIN1-UTR	This work	N/A

(*Continued on next page*)

Continued

REAGENT or RESOURCE	SOURCE	IDENTIFIER
pCMV-HA-NLS-KDM6B-IDRdel-NU	This work	N/A
pCMV-HA-KDM6B-HPdel-NU	This work	N/A
pCMV-HA-KDM6B-RBRdel-U	This work	N/A
pCMV-HA-KDM6B-HPC32mut-NU	This work	N/A
pCMV-HA-KDM6B-K1109R-NU	This work	N/A
pCMV-HA-KDM6B-K1109R-U	This work	N/A
pLKO.1-shRNA2 Control (scramble)	Sarbassov et al.[76]	Addgene Plasmid #1864
pLKO.1-shKDM6A	Agger et al.	N/A
pLKO.1-shENO1	This work	N/A
pLKO.1-shDHPS	This work	N/A
pCMV-HA-SSRP1-NU	This work	N/A
pCMV-HA-SSRP1-U	This work	N/A
pCMV-HA-SF3B4-NU	This work	N/A
pCMV-HA-SF3B4-U	This work	N/A
pCMV-HA-EIF3I-NU	This work	N/A
pCMV-HA-EIF3I-U	This work	N/A
pCMV-HA-SSBP4-NU	This work	N/A
pCMV-HA-SSBP4-U	This work	N/A
pCMV-HA-DHPS-NU	This work	N/A
pCMV-HA-DHPS-U	This work	N/A
pCMV-HA-DHPS-shResistant-NU	This work	N/A
pCMV-HA-DHPS-shResistant-U	This work	N/A
pCMV-HA-RACK1-NU	This work	N/A
pCMV-HA-RACK1-U	This work	N/A
pCMV-HA-FOXP2-NU	This work	N/A
pCMV-HA-FOXP2-U	This work	N/A
pCMV-HA-ENO1-NU	This work	N/A
pCMV-HA-ENO1-U	This work	N/A
pCMV-HA-ENO1-shResistant-NU	This work	N/A
pCMV-HA-ENO1-shResistant-U	This work	N/A
pLenti-puro-gRNA-TIAL1	This work	N/A
pET28a-KDM6B-FD	This work	N/A
pET28a-reg_IDR	This work	N/A
pET28a-reg_IDR_RBRdel	This work	N/A
Software and algorithms		
R Studio	R Project	https://www.r-project.org
SPSS Software Version 14	IBM SPSS Statistics	https://www.ibm.com/products/spss-statistics
Python version 3.10	Python Software Foundation	https://www.python.org
FIJI	Schindelin et al.[77]	https://fiji.sc/
GraphPad Prism 10	GraphPad Software	http://www.graphpad.com/scientific-software/prism
Image Studio	LI-COR	https://www.licor.com/bio/products/software/image_studio_lite/
IUPred2A	Mészáros et al.[30]	https://iupred2a.elte.hu
localCIDER	Holehouse et al.[78]	https://pappulab.github.io/localCIDER
scikit	Van der Walt et al.[79]	https://scikit-image.org
PHAST	Siepel et al.[3]	http://compgen.cshl.edu/phast
AlphaFold3	Abramson et al.[52]	https://alphafoldserver.com

(*Continued on next page*)

Continued

REAGENT or RESOURCE	SOURCE	IDENTIFIER
DAVID	Sherman et al.[32]	https://davidbioinformatics.nih.gov/tools.jsp
ChimeraX	Goddard et al.[80]	https://www.cgl.ucsf.edu/chimerax
Salmon	Patro et al.[81]	https://combine-lab.github.io/salmon
tximport	Soneson et al.[82]	https://www.bioconductor.org/packages/release/bioc/html/tximport.html
DESeq2	Love et al.[83]	https://bioconductor.org/packages/release/bioc/html/DESeq2.html
Galaxy	The Galaxy Community	https://usegalaxy.org
pheatmap	Raivo Kolde[84]	https://CRAN.R-project.org/package=pheatmap
TrimGalore	Felix Krueger[85]	https://www.bioinformatics.babraham.ac.uk/projects/trim_galore
bowtie2	Langmead et al.[86]	https://bowtie-bio.sourceforge.net/bowtie2/index.shtml
MACS2	John Gaspar[87]	https://pypi.org/project/MACS2
BEDTools	Quinlan and Hall[88]	https://bedtools.readthedocs.io/en/latest/
deepTools	Ramírez et al.[89]	https://deeptools.readthedocs.io/en/latest
nd2	Talley Lambert	https://pypi.org/project/nd2
FCS Express 7 software	De Novo Software	https://denovosoftware.com
Pear v0.9.6	Zhang et al.[90]	https://cme.h-its.org/exelixis/web/software/pear
Seqkit	Shen et al.[91]	https://github.com/shenwei356/seqkit
pLink3 v3.0.16	Chen et al.[92]	https://github.com/pFindStudio/pLink3
MaxQuant	Cox and Mann[93]	https://maxquant.org
Other		
EASY-Spray™ HPLC Columns	Thermo Fisher	Cat# ES903
Superdex 200 Increase 10/300 GL	Cytiva	Cat# 28990944

EXPERIMENTAL MODEL AND STUDY PARTICIPANT DETAILS

Cell lines

HeLa (human cervical cancer line, female origin) was previously described.[11] MCF7 (human breast cancer, female origin) and U2OS (human osteosarcoma line, female origin) were previously described.[5] All cells were maintained at 37°C with 5% CO2 injection in Dulbecco's Modified Eagle Medium (DMEM) containing 4.5 g/l glucose, 10% heat inactivated fetal bovine serum, 100 U/ml penicillin and 100 μg/ml streptomycin. These cell lines have not been authenticated.

Doxycycline-inducible TIAL1 *knockout HeLa cells (*TIAL1 *iKO)*

Doxycycline (Dox)-inducible Cas9 (iCas9) HeLa Cells were generated as previously described.[13] The iCas9 line was transduced with a lentiviral construct harboring a pair of guide RNAs either targeting *TIAL1* or non-targeting control sgRNAs. The plentiGuide-puro vector was adapted to generate these constructs, where synthetic DNA fragments were ordered from Genewiz/Azenta and inserted. The guide RNA sequences are listed in Table S6. Lentivirus was generated in HEK293T cells, and iCas9 cells were transduced followed by puromycin selection. For induction of gene knockouts, *TIAL1* iKO and control cells were treated with 100 ng/ml Dox for five days, after which TIAL1 and TIA1 expression were evaluated by western blotting.

iPSCs with partial KDM6B *3′UTR deletion*

The 731.2B iPS cell line containing Cas9 was obtained from the Stem Cell Core facility at MSKCC and cultured using a StemFlex medium (Thermo Fisher Scientific, A3349401) on a Matrigel (Corning, 354277)-coated surface in a humidified 37°C incubator with 5% CO2. To generate 3′UTR deletion cells, Cas9 expression was induced using 1 μg/ ml Doxycycline (Acros Organics, 446060050) in Stemflex media one day prior to sgRNA transfection with Lipofectamine RNAiMax (Thermo Fisher Scientific, 13778150). After two days of gene editing, the cells were detached with Accutase and passed through a 40 μm strainer to make a single cell suspension for colony formation. To increase cell viability, the cells were plated under 10 μM Y27632 in Stemflex media

and washed out on the second day. Gene editing of single colonies was validated by Amplicon Sequencing (Genewiz) and qRT-PCR analysis for *KDM6B* CDS and 3′UTR mRNA expression in three 3′UTR deletion (Udel) and three control clonal cell lines. The guide RNA sequences and primers are listed in Table S6.

METHOD DETAILS

Vector constructs

GFP-tagged constructs

For GFP-tagged constructs, pcDNA3.1-puro mGFP (monomeric GFP, A207K), which was previously reported,[11] was used, except for MYC constructs, where EGFP was used. To generate GFP-MYC, the *MYC* promoter (2780 bp; hg38, chr8:127733806-127736585) was PCR-amplified from HeLa genomic DNA and inserted between BglII and NheI sites. To generate GFP-MYC-NU, the *MYC* coding sequence (1365 bp) was PCR-amplified from HeLa cDNA and inserted between BsrGI and BamHI sites. For GFP-MYC-U, the MYC 3′UTR (473 bp) was amplified and inserted between BamHI and EcoRI of the NU construct.

To obtain GFP-KDM6A and GFP-KDM6B constructs for RNA-FISH, the coding sequences were PCR-amplified from HA-tagged constructs (see below) and inserted into the pcDNA3.1-puro mGFP vector between BsrGI and NotI or KpnI sites, respectively. The 3′UTRs were then inserted between NotI or KpnI and XhoI sites.

HA-tagged constructs

KDM6A (NM_001291416) and *KDM6B* (NM_001080424) expression constructs in the pCMV-HA backbone were obtained from Addgene (#24168 and #24167)[38] and used as NU constructs. For the U constructs, the full-length *KDM6A* 3′UTR (1368 bp) and full-length *KDM6B* 3′UTR (1274 bp) were each amplified from HeLa genomic DNA and inserted between NotI and XhoI restriction sites. For ChIP-seq, a plasmid containing NLS-KDM6Bs (amino acids 1027–1682)[38] was used as IDRdel. The NLS (PKKKRKV) was derived from SV40 large tumor antigen and was added to the N-terminus via PCR. For all other assays, IDRdel contains this NLS at the N-terminus and amino acids 1141–1682.

All other HA-tagged expression constructs were cloned into the pCMV-HA backbone using similar approaches and were used in the chemical crosslinking experiments. For NU constructs, coding sequences (CDS, lacking a start codon) of *ENO1* (1302 bp, NM_001428.5), *SSRP1* (2127 bp, NM_003146), *SF3B4* (1272 bp, NM_005850), *SSBP4* (1155 bp, NM_032637), *EIF3I* (975 bp, NM_003757), *DHPS* (1107 bp, NM_001930) and *RACK1* (951 bp, NM_006098) were PCR amplified from HeLa cDNA and inserted between KpnI and NotI, except for the *FOXP2* coding sequence (2145 bp, NM_014491), which was PCR-amplified from HEK293 cDNA. The FOXP2-NU construct also includes a C-terminal FLAG-tag (DYKDDDK), added via PCR. For the FOXP2-U construct, the full-length *FOXP2* 3′UTR (3838 bp) was inserted between NotI and XhoI sites. For the U constructs of low-valency mRNAs, the coding sequences together with the 3′UTRs (*ENO1*, 1662 bp; *SSRP1*, 2546 bp; *SF3B4*, 1497 bp; *SSBP4*, 1471 bp; *EIF3I*, 1383 bp; *DHPS*, 1228 bp; *RACK1*, 1030 bp) were directly amplified from cDNA and inserted between KpnI and NotI.

For chimeric constructs containing the *KDM6B* CDS and various 3′UTRs, 3′UTR sequences (*IDH1* 3′UTR, 850 bp; *HSPA1B* 3′UTR, 379 bp; *PIN1* 3′UTR, 490 bp; *MAP2K2* 3′UTR, 277 bp) were amplified from HeLa genomic DNA and inserted between NotI and XhoI sites of the KDM6B-NU construct.

HPC32mut construct

In the *KDM6B* CDS corresponding to the IDR, 32/210 hydrophobic residues were mutated to serine. The DNA was synthesized by GenScript and cloned into the HA-tagged KDM6B construct using HiFi DNA Assembly (NEB). The sequence is shown in Table S6.

shRNA constructs

pLKO.1 puro was used to create shRNA constructs for stable knockdown cell lines. The sequence of the shRNA against *KDM6A* was previously reported.[38] shRNA sequences against *ENO1* and *DHPS* were obtained from the RNAi Consortium at the Broad Institute. DNA oligonucleotides (Table S6) were annealed and inserted into pLKO.1 puro between SgrAI and EcoRI. As control, we used a scrambled shRNA (Addgene #1864).[76] To generate shRNA-resistant KDM6A expression constructs, eight synonymous mutations (CTATGAATCTCTAATCTT to tTAcGAgTCctTgATtcT) were introduced to the shRNA binding site of the original KDM6A plasmids using Q5 site-directed mutagenesis (NEB). shRNA-resistant DHPS and ENO1 expression constructs were generated with similar methods.

pET28a-MBP constructs

The pET28a vector containing a 6xHis-MBP tag was previously reported[12] and used to clone all constructs for recombinant protein expression, except for the JMJD3 folded domain (FD) construct, which was cloned into the original pET28a backbone. For constructs used in in-vitro thiol-thiol crosslinking, a C-terminal Strep-Tag II (SAWSHPQFEK) was included in the reverse primer used to amplify the inserts. The JMJD3 FD (aa 1141-1643) was inserted between the NheI and BamHI sites. The amino acid boundaries of the JMJD3 regulatory IDR are aa 971-1178, whereas the regulatory IDR_RBRdel (RBRdel) aa boundaries are 1081-1178. For thiol-thiol crosslinking, cysteines are necessary. Generation of the 6xHis-MBP-regIDR-Strep-Tag-II construct: As all native cysteines in the regulatory IDR are located outside of the HP region, they were mutated to serines using the NEBuilder® HiFi DNA Assembly Master Mix (NEB, E2621L) with forward and reverse primers carrying the mutations. A single cysteine was introduced in the HP region. According to AlphaFold3, E1102 is in close proximity to the folded domain in the predicted dimer. The 6xHis-MBP-regIDR-RBRdel-Strep-Tag-II

construct was generated through PCR-amplification using the mutated regulatory IDR construct as template and inserted between the NheI and BamHI sites. All constructs were verified by sequencing and all primer sequences and insert lengths are listed in Table S6.

DNA templates for RNA in vitro transcription

All DNA templates were PCR-amplified and purified by PCR cleanup. As the full-length *KDM6B* 3′UTR could not be transcribed, the sequence without the first 110 bp (1176 bp) was amplified from the pCMV-HA-KDM6B-U construct and used as *KDM6B* 3′UTR for in vitro experiments. The 3′UTR of *HSPA1B* (379 bp) was PCR-amplified from pCMV-HA-KDM6B-HSPA1B-UTR. The T7 promoter (TAATACGACTCACTATAGGG) was incorporated into the forward primers used for generating these templates.

Plasmid transfection and viral transduction

Lipofectamine 3000 (Thermo Fisher, L3000015) was used to transfect pcDNA3-GFP-MYC construct into U2OS cells. FuGENE HD (Promega, E2311) was used to transfect all pCMV-HA-derived plasmids and all pcDNA3-mGFP-KDM6B constructs into HeLa cells, except for HA-KDM6A, which was transfected into HeLa and MCF7 using Lipofectamine 3000. NU and U expression constructs for the same protein were transfected at the same molarity by default. For specific constructs requiring equalization of protein expression, the molarity was adjusted. Specifically, chimeric KDM6B constructs containing multivalent UTRs and U constructs of DHPS, SF3B4, SSRP1 and SSBP4 were transfected at a 1.3-fold higher molarity than their corresponding NU constructs. The FOXP2-U construct was transfected at a 1.5-fold higher molarity than its corresponding NU construct.

MCF7 cells stably expressing shKDM6B or HeLa cells stably expressing shDHPS or shENO1 were generated as previously described.[11] To generate virus, HEK293T cells were transfected using Lipofectamine 3000 with pCMV-dR8.2, pCMV-VSV-G, and the corresponding pLKO.1-shRNA plasmid. Viral particles were harvested 48 h after transfection and filtered through a 0.45 μm filter. MCF7 or HeLa cells grown in 6-well plates were transduced with 200 μl viral particles in the presence of 8 μg/ml polybrene. Puromycin (1 μg/ml) was added 48 h post-transduction. Cells were maintained in puromycin for at least four more days. Knockdown efficiency was validated by western blotting or qRT-PCR.

Western blotting

Cells were washed twice with PBS and lysed directly with 2x Laemmli sample buffer (Thermo Scientific, J61337.AC). The lysate was transferred to a 1.5 ml Eppendorf tube and boiled at 95°C for 10 min, followed by sonication for three times in 30s on/off cycles using a Diagenode Bioruptor. Samples were subjected to SDS-PAGE on NuPAGE 4 -12% Bis-Tris gradient gel (Invitrogen). For KDM6B, FOXP2, SSRP1 and KDM6A chemical crosslinking experiments, NuPAGE 3 - 8% Tris-Acetate protein gels were used. For thiol-thiol crosslinking *in vitro*, 6% or 8% Tris-Glycine gels were used. Membranes were blocked with Odyssey blocking buffer (LI-COR). The primary antibodies used were: anti-GAPDH (1:2000, Sigma-Aldrich, G8795), anti-α-Tubulin (1:1000, Sigma-Aldrich, T9026), anti-Actin (1:1000, Sigma-Aldrich, A2066), anti-GFP (1:2000, Abcam, ab13970), anti-HA (1:2000, Covance, MMS-101P), anti-Hypusine (1:1000, Sigma-Aldrich, ABS1064-I), anti-EIF5A (1:1000, Cell Signaling Technology, 20765T), anti-ZAK (1:1000, Thermo Fisher, A301-993A), anti-TIAL1/TIAR (1:1000, BD Biosciences, 610352), anti-TIA1 (1:1000, Santa Cruz Biotechnology, sc-166247), anti-UTX (1:2000, Bethyl, A302-374A), anti-RPLP0 (1:1000, Antibodies Online, ABIN310003), and anti-KDM6B/JMJD3 (1:1000, abcam, ab169197). The secondary antibodies used were: IRDye 680RD donkey anti-chicken (LI-COR, 926-68075), IRDye 680RD goat anti-mouse (LI-COR, 926-68070), and IRDye 800CW donkey anti-rabbit (LI-COR, 926-32213). Membranes were scanned with an Odyssey DLx Imaging system (LI-COR).

Chemical Crosslinking

Chemical crosslinking with DSG (Thermo Fisher) was performed as previous described,[94] with minor modifications. Briefly, HeLa cells were transfected with the indicated constructs. After 24 hours, cells grown in 24-well plates were washed twice with 0.5 ml PBS, and DSG in 200 μl PBS was directly added to each well. The reaction was incubated at room temperature (RT) with shaking for 30 min and quenched by adding 50 mM Tris, pH 7.5, for 15 min at RT. After discarding the buffers, cells were lysed with 2x Laemmli buffer. The samples were sonicated 3–5 times in 30s on/off cycles using a Diagenode Bioruptor and boiled at 95°C for 10 min. The crosslinked proteins were then analyzed by SDS-PAGE followed by western blotting.

For crosslinking using BS3 (Thermo Fisher) prior to mass spectrometry analysis, transfected cells from two 15-cm dishes were first lysed in a minimal buffer containing 20 mM HEPES, pH 7, 150 mM NaCl, 1% NP-40, and protease inhibitor cocktail. The lysates were triturated 20 times through a 26 Guage needle and cleared by centrifugation for 10 min at 14,000 rpm at 4°C. Crosslinking was performed on ice using 0.5 mM final BS3 and incubated for 2 h. The reaction was then quenched by Tris, and HA-tagged constructs were immunoprecipitated, eluted, and resolved on SDS-PAGE as described prior to being cut and submitted for mass spec analysis.

Crosslinking mass spectrometry

Protein digestion and peptides desalting

Excised gel sections were washed with 100 μl of 1:1 (v/v) solution of 100 mM ammonium bicarbonate (ABC) and acetonitrile (ACN). After incubation for 15 minutes, the buffer was discarded, and 500 μl of ACN was added until the gel bands were destained. The gel pieces were then dried in a SpeedVac concentrator, reduced with 10 mM dithiothreitol (DTT), and incubated for 30 minutes at 56°C. Following reduction, 100% ACN was added and incubated for 10 minutes at room temperature, then removed. Alkylation was

performed by adding 55 mM iodoacetamide (IAA) and incubating the samples in the dark for 30 minutes at room temperature. After removal of the solution, the gel pieces were washed with 100 mM ABC and incubated for 10 minutes. The buffer was discarded, and 100% ACN was added twice for 5 minutes each. The gel pieces were then dried in a SpeedVac for 10 minutes and digested overnight at 37°C with shaking using 10 μl of mass spectrometry-grade trypsin at a concentration of 25 ng/μl in 50 mM ABC. Peptides were extracted using 5% formic acid (FA)/50% ACN and incubated for 15 minutes at 37°C with shaking. Peptides were dried in a SpeedVac and resuspended in 50 μl of 0.1% FA. Peptides desalting was performed using hand-packed stage tips containing Empore C18 extraction disks, which were sequentially conditioned with 100% methanol, 80% ACN/0.1% acetic acid, and 0.1% FA twice, prior to sample loading. After loading, the stage tips were washed with 0.1% FA. Peptides were eluted twice with 80% ACN/0.1% acetic acid, dried in a Speed-Vac centrifuge, reconstituted in 0.1% FA, water-bath sonicated, and transferred to liquid chromatography vials.

Mass spectrometry analysis

Peptides were separated on a 50 cm C18 column (Thermo Fisher ES903) using a gradient from 1.6% to 4% buffer B over 2 minutes, followed by an increase to 30% buffer B over 133 minutes, and then to 90% buffer B over 3 minutes, which was held at 90% buffer B for an additional 7 minutes (buffer A: 0.1% FA in HPLC-grade water; buffer B: ACN containing 0.1% FA). Separation was performed at a flow rate of 300 nL/min using a Vanquish Neo HPLC system (Thermo Fisher Scientific).

Mass spectrometry data were acquired on an Orbitrap Fusion Lumos mass spectrometer (Thermo Fisher Scientific) using a data-dependent acquisition (DDA) method with a 2 second cycle time. The method consisted of one MS1 scan at 60K resolution, an AGC target of 400,000, a maximum injection time of 50 ms, and a scan range of 380-1500 m/z. A charge state filter was applied to include charge states 4-8. MS2 scans were acquired using stepped collision energies of 21%, 26% and 31%, with a maximum injection time of 70 ms, an isolation window of 1.6 m/z, and a resolution of 30K.

Identification of crosslinked peptides

Peptides cross-linked by BS3 were identified by pLink3 software (version 3.0.16)[92] using the following parameters: Cross-linker: BS3 (+138.068 Da); database: customized database with HA-JMJD3 sequence and reverse sequence added; enzyme: trypsin with up to 3 missed cleavages; precursor tolerance: 10 ppm; fragment tolerance: 20 ppm; fixed modification: carbamidomethyl [C] (+57.021 Da); variable modification: oxidation [M] (+15.995 Da) and deamidated [N] (+0.984 Da); filter tolerance: 10 ppm; separate false discovery rate (FDR) $\leq$5% at Peptide Pairs level.

Analysis of 3′UTR-dependent JMJD3 protein conformations

The KDM6B construct contains two proline insertions at aa 257, which were omitted in the analysis. Specifically, crosslinked residues were assigned based on the annotated JMJD3 sequence (UniProt ID: O15054-1) to one of the following JMJD3 regions: N-terminal IDR (aa 1-972), regulatory IDR (aa 973-1128), or folded domain (aa 1129-1682). Each crosslink was classified as IDR-IDR if either residue mapped within the N-terminal IDR or regulatory IDR region, otherwise the crosslink was classified as 'with folded'. Crosslinks unique to individual samples (NU vs U) were visualized using xiVIEW.[95]

SILAC-based co-IP-MS

HeLa cells were cultivated in DMEM medium supplemented with 10% dialyzed FBS and 1% penicillin and containing either "light" (L-Arginine-HCl and L-Lysine-2HCl) or "heavy" (L-Arginine-HCl (13C6, 99%; 15N4, 99%) and L-Lysine-2HCl (13C6, 99%)) stable isotope-labeled amino acids. Cells were cultivated for at least five passages before the incorporation efficiency was verified by mass spectrometry analysis to be above 99%. The 'light' HeLa cells were transfected with HA-KDM6B-NU, and the 'heavy' cells with HA-KDM6B-U construct using FuGENE. After 24 hours, the transfected cells were collected and lysed on ice for 30 min in RIPA buffer (10 mM Tris, pH 7.5, 150 mM NaCl, 0.5 mM EDTA, 0.1% SDS, 1% Triton X-100, 1% sodium deoxycholate) supplemented with protease inhibitor. HA co-IP was performed separately using light and heavy lysates following the manufacturer's protocol. 30 μl beads were used per sample. The beads were pooled and mixed with 2x Laemmli sample buffer, followed by SDS-gel electrophoresis and staining with SimplyBlue (Life Technologies).

The gel samples were divided into three gel slices and submitted to the MSKCC proteomics Core facility for SILAC mass spectrometry analysis. Specifically, gel slices were washed with 1:1 (vol/vol) solution of acetonitrile and 100 mM ammonium bicarbonate for 15 min, dehydrated with 100% acetonitrile for 10 min, and then dried in a SpeedVac for 10 min without heat, after removal of excess acetonitrile. Gel slices were reduced with 10 mM DTT for 30 min at 56°C in a thermomixer (Eppendorf), followed by incubation in 100% acetonitrile for 10 min. The buffer was discarded, and the samples were alkylated with 55 mM iodoacetamide (IAA) for 30 min in the dark. Gel slices were washed twice with 100 mM ammonium bicarbonate and 100% acetonitrile for 10 min each. Excess acetonitrile was removed, and the samples were dried in SpeedVac for 10 min without heat. The gel slices were then rehydrated on ice for 30 min in a solution of 25 ng/μl trypsin in 50 mM ammonium bicarbonate. Digestions were performed overnight at 37°C with shaking in a thermomixer. Digested peptides were collected and further extracted from gel slices with a 50 μl extraction buffer (5% formic acid/50% acetonitrile) for 15 minutes at 37°C with shaking in a thermomixer. Supernatants from both extractions were combined and dried in a SpeedVac centrifuge. Peptides were desalted using C18 resin-packed stage tips, lyophilized, and stored at -80°C until further use.

Peptides were separated on a 50 cm C18 column (Thermo Fisher ES903) using a gradient from 1% to 30% buffer B over 130 minutes, followed by an increase to 90% buffer B over 5 minutes and a hold to 90% buffer B for 10 minutes (buffer A: 0.1% FA in HPLC grade-water; buffer B: 95% ACN containing 0.1% FA). Separation was performed at a flow rate of 300 nl/min using an EASY-nLC 1200 Hplc system (Thermo Fisher Scientific).

Mass spectrometry data were acquired on a Orbitrap Fusion Lumos mass spectrometer (Thermo Fisher Scientific) using a data-dependent acquisition (DDA) method. The method consisted of one MS1 scan at 120K resolution, an AGC target of 400,000, a maximum injection time of 50 msec, and a scan range of 375-1500 m/z. A charge state filter was applied to include charge states 2-7. MS2 scans were acquired using collision energy of 27%, with a maximum injection time of 100 msec, an isolation window of 1.5 m/z, and a resolution of 30K.

SILAC mass spectrometry data were processed using the MaxQuant software (Max Planck Institute of Biochemistry; v.2.6.6.0).[93] The default values were used for the first search tolerance and main search tolerance—20 ppm and 6 ppm, respectively. Labels were set to Arg10 and Lys6. MaxQuant was set up to search the reference human proteome database downloaded from UniProt on 2024/04/19 (201,787 entries). Cysteine carbamidomethylation was specified as fixed modifications, while Methionine oxidation, acetylation of the protein N-terminus, Deamidation (NQ) and Phospho (STY) were set as variable modifications. A maximum of two trypsin missed cleavages were permitted. Searches used a reversed sequence decoy strategy to control peptide false discovery rate (FDR) and 1% FDR was set as threshold for identification. Peptide, site and protein FDR were all set to 1% with a minimum of one peptide needed for identification but two peptides needed to calculate a protein level ratio.

Immunofluorescence staining

HeLa cells were seeded on 4-well Millicell EZ Slides and transfected. After 24 hours, the transfected cells were briefly washed twice with PBS, fixed with 4% paraformaldehyde for 10 min at room temperature (RT), washed three times with PBS, and permeabilized in 0.1% Triton X-100 in PBS for 7 min. Cells were washed three times with PBST (PBS with 0.1% Tween-20) and incubated in blocking buffer (3% BSA in PBST) for 1 hour at RT. The cells were stained with the following primary antibodies diluted in blocking buffer at 4°C overnight: mouse anti-HA (1:1000, Covance, MMS-101P) and rabbit anti-H3K27me3 (1:2000, Cell Signaling Technology, 9733), or mouse anti-TIAR/TIAL1 (1:200, BD Biosciences, 610352). Cells were then washed 3x with PBST and incubated with secondary antibody in blocking buffer (goat anti-rabbit Alexa 647, 1:1000, Thermo Fisher A-21244 or donkey anti-rabbit Alexa 647, 1:1000, Thermo Fisher A-31573; donkey anti-mouse Alexa 488, 1:1000, Thermo Fisher A-21202 or goat anti-mouse Alexa 568, 1:1000, Thermo Fisher A-11004) for 1 hour at RT. Cells were washed three times with PBST, mounted with mounting media with DAPI, and a coverslip was added. Samples were then imaged using a Nikon CSU-W1 SoRa spinning disk microscope with a 63x/1.40 CFI Plan Apo oil immersion objective. All images were taken at the same laser intensity and exposure settings. For endogenous TIAL1 in HeLa, images were acquired using a 4x magnification changer for SoRa and deconvolved with default settings using NIS-elements software.

Lactate accumulation measurement

To measure the cellular activity of ENO1, shRNA-resistant HA-tagged ENO1 constructs were transfected into ENO1 knockdown or control HeLa cells. Twenty-four hours after transfection, the cells were quickly washed once with PBS, and the media replaced with DMEM, free of phenol red and FBS (Thermo Fisher, 21063029). The supernatant was harvested 30 minutes after media exchange. The lactate accumulation in the supernatant was measured using fluorometric lactate assay kit (Sigma-Aldrich, MAK570) following the manufacturer's instructions.

Detect RNA-protein interactions in cells

To test the RNA-binding ability of JMJD3 produced from different constructs in cells, irCLIP was performed as previously described with slight modifications.[49,50] HeLa cells cultured in 10 cm dishes were transfected with the indicated HA-tagged KDM6B plasmids for 24 h. Cells were then washed with PBS once, crosslinked with 254 nm UV-C light (1500 J/m^2), and lysed in 1 ml irCLIP lysis buffer (50 mM Tris pH 7.5, 150 mM NaCl, 1 mM EDTA, 1% Triton X-100, 0.1% SDS, 1X protease inhibitor). After sonication for 6 times in 30s on/off cycles, lysates were cleared by centrifugation at 5000 g for 10 min at 4°C. 1% of each sample was saved as input control. Each lysate sample was incubated with 30 μl HA magnetic beads (Thermo Fisher) for 2 h at 4°C with rotation. Beads were then sequentially washed with the following ice-cold buffers: twice with 1 ml irCLIP lysis buffer, twice with 1 ml high stringency buffer (20 mM Tris pH 7.5, 120 mM NaCl, 25 mM KCl, 5 mM EDTA, 1% Triton X-100, 1% sodium deoxycholate, 0.1% SDS), twice with 1 ml high salt buffer (20 mM Tris pH 7.5, 500 mM NaCl, 5 mM EDTA, 1% Triton X-100, 1% sodium deoxycholate), twice with 1 ml low salt buffer (20 mM Tris pH 7.5, 5 mM NaCl, 5 mM EDTA, 1% Triton X-100), and twice with 1 ml NT2 buffer (50 mM Tris pH 7.5, 150 mM NaCl, 1 mM $MgCl_2$, 0.05% NP-40). Ten percent of beads were then removed for immunoblot analysis, and the rest of the beads were resuspended in 30 μl NT2 buffer containing 0.5 μl RNase A (Thermo Fisher) and 15% PEG400 (Sigma-Aldrich) for on-bead RNase digestion at 30°C for 15 min with shaking (1200 rpm) in a Thermomixer. RNase digestion was quenched by the addition of 1 ml high stringency buffer, followed by two washes with 0.3 ml PNK wash buffer (50 mM Tris pH 7.0, 10 mM $MgCl_2$), and then resuspended in 30 μl PNK dephosphorylation mix (1x PNK buffer (NEB), 0.5 μl SuperaseIn (Thermo Fisher), 1 μl T4 PNK (NEB), 4 μl PEG400). Dephosphorylation reactions were conducted at 37°C for 60 min with shaking (1200 rpm) in a Thermomixer. Dephosphorylation mix was removed, and beads were washed with 0.3 ml PNK wash buffer. For ligation of IRDye-800–conjugated oligo to RNA crosslinked to protein, beads were resuspended in 30 μl RNA ligation mix (1x RNA ligase I buffer (NEB), 1 μl RNA ligase I (NEB), 0.5 μl IRDye800-labeled

oligonucleotide, 5 μl PEG400, and 0.5 μl SuperaseIn) and incubated for 16 hours at 16°C with shaking in Thermomixer (1200 rpm). Ligation mix was then removed, and beads were washed twice with 0.3 ml PNK wash buffer, prior to elution of RNA-protein complexes in 20 μl 1x LDS Buffer (Thermo Fisher) + 10% β-ME at 80°C for 10 min. 5 μl of eluates, as well as input controls, were then resolved by SDS-PAGE on 3-8% Tris-Acetate NuPAGE gels (Thermo Fisher) and transferred to nitrocellulose membranes. Fluorescent RNA-protein complexes in the eluates were visualized on a LiCOR Odyssey imager. The same membranes were then subjected to immunoblotting using anti-HA antibody.

Digitonin RNA-FISH

RNA-FISH against GFP was performed before and after digitonin extraction of the cytosol, as previously described.[11,13] Briefly, HeLa cells were seeded on 4-well Millicell EZ Slide and transfected with GFP-fusion constructs. Fourteen to 16 hours after transfection, cells were incubated with 400 μl of digitonin solution (40 μg/ml digitonin, 150 mM NaCl, 20 mM HEPES pH 7.4, 0.2 mM EDTA, 2 mM DTT, 2 mM $MgCl_2$) for 10 min at 4°C. The digitonin solution was aspirated, and coverslips were rinsed once with 400 μl PBS. For untreated samples, cells were briefly rinsed twice with PBS and subjected to the same RNA-FISH procedure described below. Specifically, cells were fixed with 4% paraformaldehyde for 10 min at RT, followed by two 5-minute washes with PBS and permeabilized using 1 ml of 70% ethanol in each well for 8 hours at 4°C. The slides were washed once with 1 ml wash buffer (2x SSC, 10% formamide) for 5 min at RT. A 200 μl hybridization mix containing Stellaris FISH Probes for eGFP with Quasar 670 Dye (Biosearchtech, VSMF-1015-5) was prepared and added to each well as previously reported. Slides were incubated at 37°C overnight, followed by two 30-minute washes with 1 ml pre-warmed wash buffer at 37°C. After a brief wash with PBST, slides were mounted with ProLong™ Gold Antifade Mountant with DAPI DNA stain (Thermo Fisher). Images were captured using a Nikon CSU-W1 SoRa spinning disk microscope with a 63x/1.40 CFI Plan Apo oil immersion objective. Excitations were performed sequentially using 405, 488, and 633 nm laser wavelengths. Eleven z-stacks were taken at 0.5 μm increments.

Disome assay

Monosome and disome isolation

For isolation of monosomes and disomes, HeLa cells were plated on 15 cm dishes and transfected with HA-tagged constructs. Twenty-four hours after transfection, cells were washed with 10 ml 1x PBS supplemented with 100 μg/ml CHX (Sigma Aldrich) and 10 mM $MgCl_2$. The PBS solution was aspirated, and 100 μl of ice-cold 5x lysis buffer (250 mM HEPES, pH 7.0, 50 mM $MgCl_2$, 750 mM KCl, 5% NP-40, 50 mM DTT, 500 μg/mL CHX, 125 U/ml Turbo DNase (Invitrogen) and cOmplete EDTA-free protease inhibitor (Roche)) was added. The cells were scraped from the plate, and 1 unit/μl of RNase I (Ambion) was directly added to the lysate. The lysate was transferred to a 1.5 ml RNase-free Eppendorf tube and incubated on ice for 30 min.

The cell lysates were gently triturated ten times through a 26 Guage needle and cleared by centrifugation for 10 min at 14,000 rpm at 4°C. Cleared lysates were loaded onto 10-25% sucrose gradients in sucrose buffer (50 mM HEPES, pH 7.0, 5 mM $MgCl_2$, 150 mM KCl, 100 μg/ml CHX, and EDTA-free protease inhibitor) and subjected to ultracentrifugation at 35,000 rpm in a TH-641 swinging bucket rotor (Thermo Fisher) for 3 hours at 4°C. Fourteen equal-volume fractions were collected using a Piston Gradient Fractionator (Biocomp) with continuous monitoring of RNA at UV260. Fractions 8-10 were pooled to obtain the monosome fraction and fractions 11-13 were pooled as the disome fraction.

Puromycylation and detection of puromycylated nascent proteins

To label and detect HA-tagged nascent chains in monosome and disome fractions, each fraction was incubated with 100 μM puromycin (Millipore) for 5 min at 37°C with shaking. 10% of puromycylated fractions were precipitated by TCA (TCI) and saved as input samples to adjust for total amount of ribosome loading. The remaining fractions were incubated with 20 μl of anti-HA magnetic beads (Thermo Fisher) for 2 hours at 4°C with constant tumbling. Beads were washed three times with 0.5 ml PBST and resuspended in 20 μl 2x Laemmli buffer. Immunoprecipitated puromycylated proteins were resolved on SDS-PAGE and probed using anti-puromycin antibody (1:1000, MilliporeSigma, MABE343) and anti-HA (1:2000, Covance, MMS-101P). To normalize for sample loading, total ribosome content in the input of each fraction was assessed by probing for RPLP0 using rabbit anti-RPLP0 (1:1000, Antibodies Online, ABIN310003). Band intensity of the HA-tagged nascent chain (puromycin signal co-localized with the HA signal) in each IP fraction was quantified by FIJI[77] and normalized to the RPLP0 signal from the corresponding input. This yielded the normalized abundance of HA-tagged nascent chain in each fraction. The ratio of HA-tagged nascent chain in the disome over the monosome fraction was calculated and plotted.

Test ribosome collisions by ZAK phosphorylation analysis

ZAK phosphorylation was analyzed using Phos-tag gels followed by western blotting as previously described.[56] Briefly, the cells were either irradiated at 1200 J/m^2 (UV-C) in culture media, followed by recovery at 37°C for 30 min, or left untreated. The cells were rinsed with PBS once and lysed in lysis buffer (20 mM Tris-Cl, pH 8, 150 mM KCl, 15 mM $MgCl_2$, 1% Triton X-100, 1 mM DTT) supplemented with phosphatase inhibitor cocktail (CST, 5870) and protease inhibitor cocktail (Roche). Lysates were incubated on ice for 30 minutes and cleared by centrifugation at 15,000 rpm for 10 min. A final 2x Laemmli loading buffer was added and boiled at 95°C for 5 min. The samples were resolved on 7% SDS-PAGE containing 10.7 μM Phos-tag (Wako, AAL-107) and 21.3 μM $MnCl_2$. The gels were rinsed with transfer buffer containing 1 mM EDTA at room temperature for 10 min, followed by 10 min wash with the transfer buffer without EDTA, and transferred to PVDF membranes following manufacturer's instructions. Membranes were blocked with 5% non-fat dry milk for 1 hour at room temperature, washed twice in PBST, and then probed with antibody.

iPSC to mesendoderm differentiation

The first three days of the GiWi cardiomyocyte differentiation protocol were performed.[96] Once the iPSCs reached 70% confluency, they were detached by Accutase and plated at 250,000 cells per well in a 12-well under 10 μM Y27632 ROCK inhibitor (StemCell Technologies, 100-1044) with Stemflex medium. The media without ROCK inhibitor was changed every day for two more days until cells were 90% confluent. RPMI 1640 (Thermo Fisher Scientific, 11875093) with B27 minus insulin (Thermo Fisher Scientific, A1895601) and 10 μM CHIR99021 (StemCell Technologies, 100-1042) was added during the first 24 hours, followed by a 48-hour incubation of RPMI 1640/B27 minus insulin with 2 μM CHIR99021 to maintain Wnt signaling. Induction of markers was monitored by flow cytometry.

Flow cytometry

Cells were collected at d0, d1, d2, d3 of the GiWi cardiomyocyte differentiation protocol. The cells were dissociated with 0.25% Trypsin (Thermo Fisher Scientific, 25200056) and neutralized by RPMI 1640 with 10% heat-inactivated fetal bovine serum. LIVE/DEAD™ Fixable Near IR staining (Thermo Fisher Scientific, L34994) was carried out to label the dead cells at 4°C for 30 minutes before 2% paraformaldehyde fixation at room temperature for 15 minutes. The cells were then permeabilized by 0.1% Triton X-100 prepared in FACS buffer (0.5% bovine serum albumin in PBS) at room temperature for 10 minutes and incubated with antibodies diluted in a FACS buffer at 4°C for 30 minutes. After washing out the unbound antibodies, the cells were resuspended in FACS buffer and passed through a 40-μm strainer to generate single cell suspension. Flow cytometry was performed on a CytoFLEX analyzer (Beckman Coulter) and the results were analyzed using FCS Express 7 software (De Novo Software). The antibodies used were: anti-Brachyury-APC (1:1000, R&D Systems, IC2085A), anti-EOMES-BV421 (1:1000, BD Bioscience, 567166), anti-KDM6B-FITC (1:1000, Novus, NBP1-06640F), and anti-GATA6-PE (1:5000, CST, 26452S).

RNA-seq

To identify 3′UTR-dependent MYC targets, U2OS cells were transfected with GFP-MYC constructs and FACS-sorted 24 hours post-transfection to isolate GFP-positive cells. RNA was extracted from GFP-positive cells using TRIzol according to the manufacturer's protocol and submitted to Genewiz for standard, 150 bp paired-end RNA sequencing (53-67 million reads were obtained per sample).

To identify 3′UTR-dependent KDM6A targets, endogenous *KDM6A* was knocked down with shRNAs and HA-tagged shRNA-resistant KDM6A constructs were transfected into the *KDM6A* knockdown cells. At 24 hours post-transfection, expression levels of total KDM6A and HA-tagged constructs were validated by western blotting using rabbit anti-UTX (1:2000, Bethyl, A302-374A) and mouse anti-HA (1:2000, Covance, MMS-101P) antibodies, respectively. RNA was then extracted using TRIzol according to the manufacturer's protocol and submitted to Genewiz for standard, 150 bp paired-end RNA sequencing (19-30 million reads per sample were obtained).

ChIP-seq

To analyze genome-wide 3′UTR-dependent JMJD3/KDM6B protein localization and activity, HeLa cells were co-transfected with HA-tagged KDM6B constructs and pcDNA3-mGFP at a 10:1 ratio. Twenty-four hours after transfection, cells were trypsinized, washed twice with ice-cold PBS, and stained with LIVE/DEAD fixable far-red stain (Thermo Fisher) following the manufacturer's protocol. The cells were washed twice with ice-cold PBS and fixed with 1% paraformaldehyde for 10 min at room temperature on a nutator. Paraformaldehyde was quenched with 0.125 M glycine and mixed for 5 min at RT. The cells were centrifuged at 500 g for 5 min at 4°C, washed twice with ice-cold PBS supplemented with 1% FBS and EDTA-free protease inhibitor, and sorted by FACS to collect GFP-positive cells.

ChIP was performed by the MSKCC Epigenetics Research Innovation Lab. Cells were resuspended in SDS buffer (100 mM NaCl, 50 mM Tris-HCl pH 8.0, 5 mM EDTA, 0.5% SDS, 1x protease inhibitor cocktail from Roche). The resulting nuclei were spun down, resuspended in the immunoprecipitation buffer at 1 ml per 0.5 million cells (SDS buffer and Triton Dilution buffer (100 mM NaCl, 100 mM Tris HCl pH 8.0, 5 mM EDTA, 5% Triton X-100) mixed in 2:1 ratio with the addition of 1x protease inhibitor cocktail (Millipore Sigma, #11836170001) and processed on a Covaris E220 Focused-ultrasonicator to achieve an average fragment length of 200–300 bps with the following parameters: PIP=140, Duty Factor=5, CBP/Burst per sec=200, Time = 20 min. Chromatin concentrations were estimated using the Pierce™ BCA Protein Assay Kit (ThermoFisher Scientific #23227) according to the manufacturer's instructions. The immunoprecipitation reactions were set up in 500 μl of the immunoprecipitation buffer in Protein LoBind tubes (Eppendorf, #22431081) and pre-cleared with 50 μl of Protein G Dynabeads (ThermoFisher Scientific #10004D) for two hours at 4°C. After pre-clearing, the samples were transferred into new Protein LoBind tubes and incubated overnight at 4°C with 5 μg of HA antibody (CST, #3724) and H3K27me3 antibody (CST, #9733). For normalization purposes, 2 μl of KMet SNAP-ChIP Panel (Epicypher, #191100) were added to each reaction. The next day, 50 μl of BSA-blocked Protein G Dynabeads were added to the reactions and incubated for 2 hours at 4°C. The beads were then washed twice with low-salt washing buffer (150 mM NaCl, 1% Triton X-100, 0.1% SDS, 2 mM EDTA, 20 mM Tris HCl pH 8.0), twice with high-salt washing buffer (500 mM NaCl, 1% Triton X-100, 0.1% SDS, 2 mM EDTA, 20 mM Tris HCl pH 8.0), twice with LiCL wash buffer (250 mM LiCl, 10 mM Tris HCl pH 8.0, 1 mM EDTA, 1% Na-Deoxycholate, 1% IGEPAL CA-630) and once with TE buffer (10 mM Tris HCl pH 8.0, 1 mM EDTA). Samples were then reverse-crosslinked overnight in the elution buffer (1% SDS, 0.1 M NaHCO3) and purified using the ChIP DNA Clean & Concentrator kit (Zymo Research, #D5205) following the manufacturer's instructions. After quantification of the recovered DNA fragments, libraries were prepared using the

ThruPLEX®DNA-Seq kit (R400676, Takara) following the manufacturer's instructions, purified with SPRIselect magnetic beads (B23318, Beckman Coulter), and quantified using a Qubit Flex fluorometer (ThermoFisher Scientific) and profiled with a TapeStation (Agilent). The libraries were sent to MSKCC Integrated Genomics Operation core facility for sequencing on an Illumina NovaSeq 6000 (aiming for 30-40 million 100 bp paired-end reads per library).

qRT-PCR

RNA was isolated from cells using TRI Reagent (Invitrogen) following the manufacturer's protocol. RNA was reverse transcribed using qScript™ cDNA SuperMix (Quanta Bioscience). cDNA was diluted 5x and used for real-time PCR with gene-specific primers in the presence of PowerUp SYBR Green Master Mix (Life Technologies) by QuantStudio 6 Real-Time PCR system (Applied Biosystems). RPLP0 or GAPDH was used as housekeeping genes for normalization control. Primer sequences are listed in Table S6.

Protein purification

All expression constructs were transformed into BL21 *E. coli* (NEB) for protein expression. With the exception of the regulatory IDR, all proteins were purified using TALON resin under native conditions, followed by size exclusion chromatography. Specifically, a fresh colony was used to inoculate an overnight culture in 5 ml LB/kanamycin media and shaken vigorously at 250 rpm at 37°C. The overnight culture was diluted in 500 ml LB media containing 50 mg/l kanamycin and grown at 37°C until OD600 reached 0.6-0.8. Protein expression was induced by adding 0.5 mM IPTG, and the bacteria were cultured at 18°C overnight. Bacteria were harvested by centrifugation at 6,000 g for 15 min. The pellet was resuspended in 30 ml cold lysis buffer (50 mM sodium phosphate pH 7.4, 600 mM NaCl, 1 mM PMSF), supplemented with 10 mg lysozyme (Life Technologies), 1x Halt protease inhibitor cocktail (Thermo Fisher), and 1 mg DNase I (Roche). After incubation on ice for 30 min, bacteria were sonicated on ice for 3 min 30 seconds with on/off intervals of 1 and 3 s (Misonix S-4000). The lysate was cleared by centrifugation at 38,000 g at 4°C for 30 min.

5 ml TALON metal affinity resin (TaKaRa Bio) was equilibrated with five column volumes of native lysis buffer. The supernatant of cleared bacteria lysate was transferred to a new 50 ml Falcon tube and incubated with TALON resin with rotation at 4°C for 2 hours. The slurry was transferred into a gravity column and washed with 10 column volumes of native wash buffer (50 mM sodium phosphate pH 7.4, 600 mM NaCl, 10 mM imidazole). The protein was eluted with five column volumes of elution buffer (50 mM sodium phosphate pH 7.4, 600 mM NaCl, 200 mM imidazole).

The TALON-eluted protein was buffer-exchanged into protein storage buffer (25 mM Tris-Cl pH 7.4, 150 mM NaCl, 1 mM TCEP, 5% glycerol, and 0.01% Tween-20) using centrifugal filters with a 30 kDa cutoff (Pall) and concentrated to 1 ml. The concentrated protein was spun down at 20,000 g for 5 min at 4°C, and the supernatant was loaded onto a Superdex 200 Increase 10/300 column using the AKTA Purifier system (Cytiva). Peak fractions were collected, aliquoted, and snap-frozen in liquid nitrogen for storage at -80°C.

As the 6xHis-MBP-StrepII-tagged regulatory IDR protein domain degrades on the size exclusion column, a two-step purification was performed. Specifically, the regulatory IDR was first purified using TALON resins under native conditions as described above. The eluted protein was concentrated to 10 ml using a 30 kDa cutoff centrifugal filter. The concentrated protein was passed through 2.5 ml of pre-equilibrated Strep-Tactin® 4Flow® high-capacity resin (IBA Lifesciences) twice. The protein-bound beads were then washed with 5 column volumes of PBS and eluted with 5 column volumes of PBS supplemented with 10 mM desthiobiotin (Sigma Aldrich). The eluted regulatory IDR was buffer-exchanged into the protein storage buffer by using a 10 kDa cutoff centrifugal filter, aliquoted, and snap-frozen in liquid nitrogen for storage at -80°C. Protein concentrations were determined by BCA assay (Thermo Fisher). The integrity of the purified protein was examined by SDS-PAGE and Coomassie blue staining.

RNA *in vitro* transcription

All RNAs were prepared by *in vitro* transcription using the T7 MEGAscript kit (Invitrogen). 250 ng of PCR-amplified DNA template was used for each 20 μl reaction. For Cy5 labeling, Cy5-UTP (Enzo life sciences, ENZ-42506) was added at a ratio of 1:300 labeled UTP:unlabeled UTP. The reaction mix was prepared following the manufacturer's protocol and incubated at 30°C for 6 hours. The products were then treated with Turbo DNase provided in the kit and incubated at 37°C for 15 min. The integrity and sizes of the RNAs were verified using agarose gel electrophoresis. All RNAs were precipitated with LiCl overnight at -20°C. The RNAs were pelleted by centrifugation at 20,000 g for 20 min at 4°C, washed with 1 ml of 70% ethanol, redissolved in nuclease-free water, aliquoted, and stored at -80°C. RNA concentration was measured by NanoDrop.

Fluorescence polarization assay

To measure the RNA binding affinity, MBP-tagged protein domains were serially diluted using dilution buffer (25 mM Tris-Cl pH 7.4, 150 mM NaCl, 0.01% Tween-20, and 400 U/ml SUPERase·In™ RNase Inhibitor (ThermoFisher). Then, Cy5-labeled RNA (2.4 ng/μl) was added to the diluted proteins for a final reaction volume of 20 μl. All experiments were performed in triplicate. Reactions were incubated in a flat-bottom black 384 well-plate (Revvity) on a rocker at RT for 1 hour. Then, fluorescence polarization was measured using an Infinite M1000 Pro (Tecan) with the following parameters in i-control: excitation wavelength: 635 nm; emission wavelength: 665 nm; excitation/emission bandwidth: 5 nm; gain: 100 (manual); number of flashes: 30; settle time: 5 ms; Z-position: 24836 μm (manual); G-Factor: 1.1 (manual). Each sample was measured three-times, and the mean values were used for binding affinity calculations. Binding curves were fitted to the fluorescence polarization data using the nonlinear regression "One site – Total" model in Prism 10.

In vitro thiol-thiol crosslinking

To perform thiol-thiol crosslinking, JMJD3 regulatory IDR (5 μM) and FD (5 μM) were mixed with Cy5-labeled RNA (6 ng/μl) on ice in an assay buffer containing 25 mM Tris-Cl pH 7.4, 150 mM NaCl, and 0.01% Tween-20. BMOE (Thermo Fisher) was added to a final concentration of 5 μM in a total reaction volume of 20 μl. After 1 hour of incubation at 25°C, the reactions were quenched with 10 μl of 6x Laemmli SDS sample buffer. The samples were boiled at 95°C for 7 min and loaded onto 6% and 8% Tris-Glycine gels to resolve the dimer or monomer bands, respectively. Western blot was then performed, and proteins were probed with Streptavidin-680 (LI-COR, 1:3000 dilution).

mRNA feature analysis

The human MANE gene annotations (GRCH38/hg38) were used for all analyses.[97]

PhyloP sequence conservation in 3′UTRs

The genome-wide phylogenetic *P* value (phyloP conservation score) was obtained from the PHAST package for multiple alignments of 99 vertebrate genomes with the human genome in a form of a bigwig file. The genome-wide phyloP score was mapped to the 3′UTR boundaries of the human GTF (genome-build: GRCh38.p14, genome-build-accession: GCA_000001405.29), and the phyloP conservation values for 3′UTRs were obtained. To determine the number of conserved nucleotides in human 3′UTRs, we used a minimum phyloP score ≥ 2 and designated them as conserved, if at least four consecutive nucleotides had phyloP scores above this cutoff. If a given 3′UTR contains more than 150 conserved nucleotides, is it considered highly conserved. Non-conserved 3′UTRs contain zero conserved nucleotides, given our criteria. The sum of conserved nucleotides for each 3′UTR is listed in Table S1.

Enriched motifs in HC and NC 3′UTRs

To identify enriched 6-mer motifs in HC vs NC 3′UTRs, we used HOMER.[98] To identify motifs enriched in HC 3′UTRs, we used all HC 3′UTRs and compared them against the rest of the 3′UTRs. For motifs enriched in NC 3′UTRs, we used all NC 3′UTRs and compared them against the rest of the 3′UTRs. For all obtained significant motifs ($P < 0.05$), we calculated the motif frequencies within the groups of HC 3′UTRs and NC 3′UTRs by normalizing them by the total number of nucleotides in each group. Shown is the fold-change in motif frequency between HC and NC 3′UTRs.

mRNA features

3′UTR length, CDS length, and AU content were obtained from MANE and shown in Table S1.

Predicted RNA binding site density

As RNA valency describes accessible RNA-RNA binding sites in an RNA, we calculated the number of all possible 5-mer binding sites in a given RNA. We used all consecutive 5-mers and asked how often the reverse complement sequence is encountered in the RNA. We used Watson-Crick base pairing and allowed G-U wobble binding. We calculated the sum of all such putative binding sites in a given 3′UTR. To normalize for RNA length, we divided this number by (3′UTR length)^2 to obtain 'binding site density' or BSD. As this value does not account for accessibility of the putative binding sites, it describes RNA valency less well than A5/U5.

Mean MFE values of predicted RNA secondary structures obtained by RNAfold

We calculated the average minimum free energy (MFE) values for each 3′UTR obtained from RNAfold.[99] As MFE values depend on RNA length, we segmented each 3′UTR into 200-nucleotide-long windows with a 100-nucleotide overlap between consecutive windows. We used RNAfold to obtain the MFE values for each 200-nucleotide-long fragment and report the average MFE values obtained from all windows of a given 3′UTR in Table S1. Terminal 3′UTR windows shorter than 200 nucleotides were not included in the analysis.

A/U homopolymers (A5/U5)

Homopolymer stretches with at least five consecutive As or five consecutive Us, also called A5/U5, were counted in each 3′UTR and the sum is reported in Table S1. Ten consecutive As or Us were counted as two.

mRNAs enriched in cytosol or cytoplasmic mesh-like condensates

The list of cytosol-enriched mRNAs were obtained from Horste et al.[13] and Chen et al.[14] and are listed in Table S1.

CLIP peaks of condensate-enriched RNA-binding proteins

These values were previously published[13] and listed in Table S1.

Identification of the best surrogate marker for RNA valency

As RNA valency describes accessible RNA-RNA binding sites in an RNA,[12] Spearmen correlation coefficients between several parameters, including 3′UTR length, AU content, BSD, A5/U5, mean MFE, NED (3′UTR length-normalized ensemble diversity (NED) values[12]), condensate vs cytosol mRNA classification, and 3′UTR phyloP conservation scores were calculated (Table S4). All values are reported in Table S1. This analysis revealed that A5/U5 correlated best with both 3′UTR length and weak RNA secondary structure (less negative mean MFE values). Therefore, A5/U5 was chosen as the surrogate marker for human multivalent mRNAs that strongly differ in length.

Codon usage

Translation rates can differ across codons. Based on two datasets,[100,101] we classified codons into optimal and non-optimal classes, and analyzed the ratio of non-optimal to optimal in the wildtype *KDM6B* CDS as well as in our mutants. We did not observe a difference in usage of non-optimal codons (Table S5).

Protein feature analysis

Identification of IDRs and folded domains

The coding sequences obtained from MANE gene annotations were translated into amino acids. A wrapper script was used to run IUPred2A.[30] All amino acids with IUPred2A score $\geq$ 0.33 were defined as IDRs and all amino acids with IUPred2A score < 0.33 were defined as folded domains and listed in Table S1.

To determine the longest IDR of each protein, we used a minimum of 30 amino acids and required $\geq$ 90% of amino acids to have IUPred2A values of $\geq$ 0.33. The longest continuous region that meets these criteria is annotated as longest IDR of a protein (Table S1). The longest folded domain of a given protein is calculated in a similar fashion, using a minimum of 30 amino acids and requiring $\geq$ 90% of amino acids to have IUPred2A values of < 0.33.

pLDDT (predicted Local Distance Difference Test) scores were obtained from AlphaFold and amino acids with pLDDT scores < 0.8 were considered unstructured. These values were used in Figures 1G and S1B.

Hydrophobic amino acid clusters (HPCs) in IDRs

The longest IDR of each protein was scanned with a sliding window of four amino acids. If a window contains at least three hydrophobic amino acids (VILMCWYF), it is counted as hydrophobic sticker. An HPC is defined as two hydrophobic stickers with 20 (or less) amino acids of distance between them. HPCs are listed in Table S1.

PhyloP sequence conservation in HPCs and surrounding IDRs

This analysis was performed for all MANE transcripts, whose CDS corresponds to uniprot amino acid sequence isoform 1. The corresponding MANE coordinates of amino acid positions of HPCs were determined and the average phyloP scores within these regions as well as in the surrounding IDR amino acids, present in the longest IDR were calculated. The obtained numbers are listed in Table S1.

Basic patches in IDRs and folded domains

Basic patches are assigned to regions with window size of 10 with a net charge per residue $\geq$ 0.3. This means that within a stretch of 10 amino acids, we require four positively charged amino acids (K or R), if there is one negatively charged amino acid (E or D) present. The obtained numbers are listed in Table S1.

JMJD3 net charge per residue (NCPR), hydrophobicity and phyloP values

The net charge per residue for JMJD3 was calculated with localCIDER[78] using a step size of 50. Hydrophobicity values per residue were obtained from Protscale.[102] The phyloP nucleotide scores for the *KDM6B* CDS were plotted with a sliding window of 50.

Gene ontology analysis

Gene ontology analysis was performed using DAVID.[32] Bonferroni-adjusted *P* values are reported.

Protein structure prediction

JMJD3 dimer structures were generated using the AlphaFold3 online server with default parameters. For each full-length protein, five structures were generated, and the highest-ranked structure was selected and rendered using UCSF ChimeraX (v1.9).[80]

RNA-seq analysis

Raw sequencing reads were quantified using Salmon (v1.10.1).[81] The GENCODE release v44 and v47 basic annotations were used as the references for MYC RNA-seq and UTX RNA-seq, respectively. Transcript-level data was imported using tximport (v1.22.0),[82] and differential gene expression analysis was performed using DESeq2 (v1.38.3 or Galaxy Version 2.11.40.8+galaxy0).[83] Only protein-coding genes defined by the GENCODE annotation were included in the following analysis.

To identify genes regulated by MYC-NU or MYC-U, each condition was compared against the GFP-only control. We focused on mRNAs expressed in the GFP sample with mean TPM (transcripts per million) > 3. Differentially expressed genes have a $|\log2FC| > 0.3$ and an adjusted *P* value < 0.1 in at least one of the tested conditions. Hierarchical clustering was performed on differentially expressed genes identified in either condition. The clustering was based on the z-score of the mean TPM value for each mRNA obtained from replicates and utilized the "ward.D" agglomeration method in R. 3′UTR-dependent groups were then defined using the obtained clusters and are presented in Table S2. The heatmap was visualized using the pheatmap (v1.0.13) package in R.[84]

For the UTX RNA-seq analysis, UTX-regulated genes were first identified by comparing samples expressing shRNA targeting *KDM6A* to those expressing a scrambled control shRNA. Transcripts with a *P* value < 0.05 according to DESeq2 were considered significantly regulated. Based on the direction of change, these were classified as either "UTX-activated" (downregulated upon *KDM6A* knockdown) or "UTX-repressed" (upregulated upon *KDM6A* knockdown).

To identify genes rescued by expression of either the KDM6A-NU or KDM6A-U construct, we first filtered for robustly expressed genes, requiring a mean TPM > 7 in either the shCtrl or shKDM6A samples. Next, we selected genes that exhibited partial rescue, defined as those whose expression in KDM6A-NU or KDM6A-U transfected samples shifted back towards the levels observed in the shCtrl samples. mRNAs were divided into "UTX-activated" and "UTX-repressed" categories and clustered separately. Hierarchical clustering was performed on the z-scored mean TPM values using the "average" linkage method in R. 3′UTR-dependent groups were then defined using the clustering results and presented in Table S2.

ChIP-seq analysis

Raw sequencing reads were trimmed and filtered for quality and library adapters using version 0.4.5 of TrimGalore,[85] with a quality setting of 15 and running cutadapt (v1.15) and FastQC (v0.11.5). Reads were aligned to human assembly hg38 with version 2.3.4.1 of bowtie2 (http://bowtie-bio.sourceforge.net/bowtie2/index.shtml) and were deduplicated using MarkDuplicates in version 2.16.0 of Picard Tools.[86] To ascertain enriched regions, MACS2[87] was used with a *p*-value setting of 0.001 and run against a matched control for each condition. A peak atlas was created by combining the superset of all peaks using the 'merge' function in the BEDTools suite v2.29.2.[88] Read density profiles were created using deepTools 'bamCoverage' v3.3.0,[89] normalized to 10 million uniquely mapped reads and with read pileups extended to 200 bp. For histone modification data, ChIP signal was scaled to the inverse of the normalized counts to reads aligning to H3K27me3-modified synthetic nucleosome spike-in barcodes. H3K27me3 enrichment was classified as two-fold enrichment of spike in signal in comparison with control. Peak-gene associations were created by assigning all intragenic peaks to that gene, while intergenic peaks were assigned using linear genomic distance to transcription start site. Composite and tornado plots were created using deepTools v3.3.0 by running computeMatrix and plotHeatmap on normalized bigwigs with average signal sampled in 25 bp windows and flanking region defined by the surrounding 2 kb for HA signal and 10 kb for H3K27me3. Motif signatures were obtained using Homer v4.5 (http://homer.ucsd.edu).

Immunofluorescence staining analysis

To analyze JMJD3/KDM6B protein abundance and protein activity after transfection of HA-tagged KDM6B constructs at the single-cell level, we loaded the obtained images using the nd2 (v0.10.0) package and processed them with the scikit-image package (v0.22.0) in Python.[79] We first generated nuclear masks from DAPI channel grayscale images. Specifically, images were denoised using a Gaussian filter (sigma = 4, truncate = 4). Then, we created binary masks using each image's mean intensity as a threshold. The masks were further refined through binary closing/opening, hole filling and removal of border-touching objects. Next, nuclei were segmented using the watershed algorithm, seeded by local maxima. Lastly, fluorescence signals from the H3K27me3 and HA channels were quantified using the refined masks.

The median fluorescence H3K27me3 signal obtained from untransfected cells (HA < 500 units) of each sample were used for normalization.

For HA signals, the median intensity obtained from the NU-transfected cells or, in the cases of deletion mutants, from the FL-transfected cells of each sample was used for normalization. The median intensity from U-transfected Ctrl cells was used for normalization when comparing Ctrl vs. dox-inducible *TIAL1* knockout cells. The median intensity from IDRdel-transfected cells was used for normalization when comparing IDRdel and HPC32mut.

Digitonin RNA-FISH analysis

To determine the fraction of mRNA transcripts retained in the cytoplasm after digitonin treatment, we calculated the ratio of mean fluorescence intensity in the cytoplasm of digitonin-treated cells over untreated cells. Specifically, we used FIJI[77] to generate masks for the whole cell and nucleus using the maximum projection of fluorescence signals from RNA-FISH and DAPI channels, respectively. Next, maximum projection of RNA-FISH signals were quantified using the whole cell and nucleus masks. Mean cytoplasmic signals were calculated by subtracting total nuclear signals from total whole cell signals, divided by the cytoplasmic area. At least six fields of view were quantified for each sample from each replicate. For each experiment, mean cytoplasmic RNA-FISH signal in each digitonin-treated cell was divided by the median of the mean cytoplasmic RNA-FISH signal from all untreated cells. At least three independent experiments per construct were performed.

Amplicon seq analysis

Amplicon sequencing for iPSC 731.2B-KDM6B Udel clones was performed by Genewiz. Paired-end reads were merged using Pear v0.9.6 with default settings.[90] Unique reads were counted with Seqkit.[91]

QUANTIFICATION AND STATISTICAL ANALYSIS

Statistical parameters are reported in the figures and figure legends, including the definitions and exact values of *N* and experimental measures (mean ± SD or SEM or boxplots depicting median, 25th and 75th percentile (boxes) and 5% and 95% confidence intervals (error bars)). All *P* values are listed in Table S7. Transcriptome-wide feature comparisons were performed using a two-sided Mann-Whitney test or a Wilcoxon test in SPSS. For experimental data, *P* values were calculated using GraphPad Prism. Statistical analysis used unpaired, two-sided t-test for bulk analysis, and two-sided Mann-Whitney test for comparison of values obtained at single-cell levels.